Using motionally-induced electric signals to indirectly measure ocean velocity: Instrumental and theoretical developments

Zoltan B. Szuts[b]

[a]*Max-Planck Institut fü Meteorologie, Bundesstraße 53, 20146 Hamburg, Germany. ph: +49-40-411-73-152, fax: +49-40-411-73-366,*
[b]*Most of this work was undertaken at the Applied Physics Lab, University of Washington, 1013 NE 40th St, Seattle, WA 98105*

Abstract

The motion of conductive sea water through the earth's magnetic field generates electromagnetic (EM) fields through a process called motional induction. Direct measurements of oceanic electric fields can be easily converted to water velocities by application of a first order theory. This technique has been shown to obtain high quality velocities through instrumental advances and an accumulation of experience during the past decades. EM instruments have unique operational considerations and observe, for instance, vertically-averaged horizontal velocity (from stationary sensors) or vertical profiles of horizontal velocity (from expendable probes or autonomous profiling floats). The first order theory describes the dominant electromagnetic response, in which vertically-averaged and vertically-varying horizontal velocities are proportional to electric fields and electric currents, respectively. After discussions of the first order theory and deployment practices, operational capabilities are shown through recently published projects that describe stream-coordinate velocity structure of the Antarctic Circumpolar Current, quickly-evolving overflow events in the Denmark Strait, and time-development of momentum input into the ocean from a hurricane.

A detailed analysis of the Gulf Stream at its separation point from the continental slope serves as a case study for interpreting EM measurements, including the incorporation of geophysical knowledge of the sediment. In addition, the first order approximation is tested by the many features at this location that contradict the approximation's underlying assumptions: sharp horizontal velocity gradients, steep topography, and thick and inhomogeneous sediments. Numerical modeling of this location shows that the first order assumption is accurate to a few percent (a few cm s^{-1}) in almost all cases. The errors in depth-varying velocity are $< 3\%$ (1–3 cm s^{-1}), are substantiated by the direct observations, and can be corrected by iterative methods. Though errors in the depth-uniform velocity are < 2 cm s^{-1} ($< 10\%$) at all locations except for the upper continental slope, where apparent but unresolved meander events in water shallower than 500 m can generate depth-uniform errors of order 30%, there are not sufficient observations to confirm these errors directly. Errors in the first order approximation at this location show no non-linear increase due to the joint effect of steep topography and horizontal velocity gradients. Using motional induction in the world's oceans, aside from stationary measurements when depth-uniform ocean currents meander across topography, these results suggest that the first order approximation is accurate to within 1–2 cm s^{-1} or less in almost all regions of the ocean, an error similar to the instrumental accuracy of EM instruments.

Keywords: current measurement, electric currents, electric fields, velocity profilers, motional

induction, USA, North Carolina, Cape Hatteras, Gulf Stream

1. Introduction

Seawater moving through the earth's magnetic field generates electric signals in the ocean through a process called motional induction. Measuring the electric response is a convenient way to indirectly measure ocean velocity. This technique has developed significantly over the past decades and is currently capable of obtaining high quality velocity measurements with unique operational benefits. Technological advances and accumulated experience behind the success of this technique have not been summarized in a readily accessible format, however, and so reviewing current practices is the first goal of this article.

Despite these observational advances, however, the theory of motional induction has not been critically examined when first order assumptions of broad ocean currents and a horizontal seafloor are invalid. To confidently interpret measurements taken in more complex locations, such as near ocean margins where energetic ocean currents flow over steep bathymetry, it is necessary to quantify higher order processes involved in motional induction. A detailed study of the higher order terms in motional induction is the second goal of this article.

The assumption of ocean currents with large width-scales flowing over nearly horizontal bathymetry leads to a dominant and one-dimensional (1D) relationship in the vertical between velocity and electrical signals, which will be called interchangeably a first order or 1D approximation. Physically, the first order approximation is based on water depth being much shorter than horizontal scales, which restricts electric fields and electric currents to flow in a vertical plane. Verification of the 1D approximation against independent velocity measurements (Spain and Sanford, 1987; Luther et al., 1991; Polzin et al., 2002) has proven it to hold within measurement accuracy, though often the reference velocities have lower vertical resolution than the electromagnetic instruments. Instrumental and observational techniques developed through such studies are mature but poorly distributed in oceanography.

Many regions of the ocean with important physical processes strongly violate the 1D assumptions, however, either because of steep bathymetry or fine-scale velocity features. A perturbation analysis treatment of motional induction by Sanford (1971) found that sloping topography and horizontal velocity gradients are only important to second order, though formally this result assumes *a priori* that gradients are weak. On one hand, electric field observations in regions that break the 1D assumptions (Spain and Sanford, 1987; Althaus et al., 2003) have not indicated any observable differences with independent velocity measurements. On the other, recent theoretical work quantified the inaccuracy of the 1D approximation for either extremely narrow velocity features (Szuts, 2010a, hereafter SzI) or extremely steep topography (Szuts, 2010b, hereafter SzII) and found small but measurable errors. In the real ocean, steep topography strongly influences the velocity field, and thus errors in such regions are not expected to simply be a linear combination of the results from SzI and SzII.

In a region where the 1D assumptions are invalidated by steep bottom topography, sharp horizontal velocity gradients, and other factors, I quantify the accuracy of the first order approximation. The study is motivated by observations collected across the Gulf Stream at its separation

Email address: zoltan.szuts@zmaw.de (Zoltan B. Szuts)

point from the continental margin. An electromagnetic numerical model (Tyler et al., 2004) is used to resolve the complexities present at Cape Hatteras. With both bottom topography and horizontal velocity gradients present at the same location, their joint perturbation to the 1D approximation is quantified and compared to the observations.

This article starts with a review of motional induction and its application for calculating water velocity. The topic is introduced with a brief historical overview of this technique in physical oceanography and in related fields of geophysics (section 2). Then the theory and physical basis are presented, both for the 1D approximation and for higher order perturbations (section 3). Application of the theory to field measurements leads into three examples of observational capabilities from recent field programs (section 4).

Building on the earlier sections, the accuracy of the 1D approximation is analyzed and quantified at Cape Hatteras (section 5). Initial interpretations of the observations (section 5.2) find that the 1D approximation is not entirely sufficient at this location. An electromagnetic numerical model (Tyler et al., 2004) is applied at Cape Hatteras (section 5.3) to calculate the complete motionally-induced response. Through comparing the model results to the observations (section 5.4), the higher order perturbations are quantified and can be used to correct the initial interpretation of the observations. The implications of these results are discussed last (sections 5.5 and 5.6).

2. Historical Background of Motional Induction

The principle of motional induction dates back to the beginning of the study of electromagnetism itself. Faraday conducted the first attempt at observing water motion from electromagnetic fields by suspending electrodes in the Thames River in an attempt to measure tidal flow (Faraday, 1832), but his attempt suffered from insufficiently accurate instruments. Advances in electronics by the mid 20th century enabled the weak signals to be measured for scientific purposes and prompted further development of the theory (Stommel, 1948; Longuet-Higgins et al., 1954). Initial interpretations of electric field observations (von Arx, 1950; Wertheim, 1954) were hampered by incomplete theory and by lack of independent velocities for comparison.

Theoretical development over the next decades allowed a better interpretation of the electromagnetic signals. For instance, Sanford (1971) developed a general and three-dimensional (3D) interpretation of motional induction, while Filloux (1967) and Larsen (1968) considered the effect of deep earth structure on tidal and geomagnetic electromagnetic signals. Although there was a greater theoretical basis for interpreting observations, the number of observations was still very limited. Cable studies (Bowden, 1956; Hughes, 1969; Robinson, 1976; Prandle, 1979) showed a strong ocean signal, but discrepancies with the expected velocities were not explained in a satisfactory manner.

Since then, development of specially-suited instruments and detailed comparison with independent velocity measurements have led to proven successes of the method. Accurate measurements have been made with cables (Larsen and Sanford, 1985; Baringer and Larsen, 2001; Kim et al., 2004; Nilsson et al., 2007), profiling instruments (Sanford et al., 1982; Sanford et al., 1985), bottom electrodes and magnetometers (Chave et al., 1989; Luther et al., 1991; Chave et al., 1997; Meinen et al., 2002, 2003), and Lagrangian drifting instruments (Sanford et al., 2011; Szuts and Sanford, in review, 2011). Various aspects of the theory have been further refined: Chave and Luther (1990) for a decomposition with spherical functions, showing that 1D oceanic electric fields (EFs) are averaged horizontally in space; and Tyler and Mysak (1995b,a) for application to a global reference frame. Numerical modeling of motional induction in the

ocean has been well established (Flosadóttir et al., 1997; Tyler et al., 2003; Vivier et al., 2004; Manoj et al., 2006).

Electromagnetic fields are also the focus of multiple subdisciplines of geophysics. The fluctuating solar wind hitting the earth's magnetosphere and ionosphere generates time-varying electromagnetic signals. Planetary researchers are interested in these outer- and upper-atmosphere fields in and of themselves, one effect of which is creating hazardous electric environments for satellites and for ground-based communication and power networks. Solid earth geophysicists measure the downward propagating EM signals that dissipate into the earth and ocean to invert for subsurface electrical structure (e.g. Filloux, 1967; Aprea et al., 1998). Because the ionospheric signals are relatively high-frequency and thus are greatly attenuated in the ocean, related techniques using active controlled-source electromagnetics (CSEM) are necessary for imaging deep ocean sedimentary structure and are widely used for research and exploration purposes (Edwards, 2005; Constable and Srnka, 2007; Evans, 2007). These remote imaging methods complement the use of electromagnetic measurements in bore holes to characterize the sediment and its hydrocarbon content.

As both geomagnetic and oceanic signals can be the same order of magnitude in certain situations (Maus et al., 2006), despite their general separation into fluctuating and quasi-static components, the removal of extraneous signals depends on the sampling method and on the phenomena of interest and thus requires a knowledge of all sources. As the focus here is on the oceanic source, this overview provides an entry point into the geophysical literature, while, in the second half of the article, geophysical data aid in interpreting the oceanic sources at Cape Hatteras.

3. Theory of Motional Induction

Electric fields occur in the ocean from the motion of conductive salt-water through the earth's magnetic field, a process generally called motional induction. The thin aspect ratio of the ocean allows for great simplification from the 3D governing equations, as do other assumptions mentioned below.

3.1. First order approximation

The dominant response restricts electric currents and electric fields to the vertical plane. A toroidal circuit is generated that involves, for example, electric currents moving in one direction in the surface intensified oceanic flow, with weaker return electric currents in the slower water and sediment beneath.

There are two aspects of the dominant response, its electric field and its electric current. The electric field is depth-uniform and is generated by the vertically-averaged velocity, while the electric current density divided by electric conductivity is depth-variable and proportional to the vertical profile of horizontal velocity. Since the electromagnetic fields of the first order approximation involve only the vertical dimension — either averages or variations in the vertical of horizontal velocity — the approximation is one-dimensional.

This section follows the derivation of Sanford (1971), so that later his form of the higher order terms can be discussed. His analysis makes use of a number of assumptions that include: a horizontal ocean bottom (H) with small topographic perturbations (h, such that $h/H \ll 1$), velocity width scales (L) much larger than bottom depth ($H/L \ll 1$), predominantly horizontal oceanic velocity ($\boldsymbol{v} = (u, v, 0)$), distant lateral boundaries, a layer of underlying sediment that

has a uniform electrical conductivity, and small time variations. Theoretical studies by Larsen (1968, 1971), Chave and Luther (1990) and Tyler and Mysak (1995a) treat additional aspects of the theory of motional induction.

Although it is readily shown that self-induction, electric currents induced by time variations of the first order magnetic fields, is negligible compared to the earth's magnetic field (Sanford, 1971; Chave and Luther, 1990), a less evident process is inductive coupling between the ocean and the conductive mantle. For the time being only slowly-changing water motion with no inductive coupling will be considered, because the electromagnetic signals so generated can be treated as quasi-static. This restriction on frequency will be refined below.

In the quasi-static limit, the horizontal electric field $\boldsymbol{E}_h$ is

$$-\boldsymbol{E}_h = \nabla_h \phi = \boldsymbol{v} \times F_z \hat{\boldsymbol{k}} - \boldsymbol{J}_h/\sigma \qquad , \tag{1}$$

where ϕ is electric potential, $\boldsymbol{v}$ is oceanic velocity, F_z is the vertical component of earth's magnetic field, σ is electrical conductivity, and $\boldsymbol{J}_h$ is horizontal electric current density. Conventions for the rest of the article are that a subscript h denotes the horizontal components and that $(\hat{\imath}, \hat{\jmath}, \hat{\boldsymbol{k}})$ point eastward, northward, and upward.

For the 1D approximation, it is assumed that $\boldsymbol{J}_h$ at a given location (x_0, y_0) is solely caused by depth-variations of the horizontal velocity $\boldsymbol{v}_h(x_0, y_0, z)$. The form of $\boldsymbol{J}_h/\sigma$ under the previously mentioned assumptions is

$$\boldsymbol{J}_h/\sigma = (\boldsymbol{v} - \overline{\boldsymbol{v}}^*) \times F_z \hat{\boldsymbol{k}} \quad , \tag{2}$$

with

$$\overline{\boldsymbol{v}}^* = \int_{-H}^{0} \sigma \boldsymbol{v} \, \mathrm{d}z' \Big/ \int_{-H_s}^{0} \sigma \, \mathrm{d}z' \quad . \tag{3}$$

The seafloor is located at $z = -H$, and the bottom of the sediment layer is at $z = -H_s$. Although the water conductivity $\sigma(z)$ varies in the vertical, the conductivity of the sediment σ_s can be assumed uniform. For the 1D approximation, it is sufficient to parameterize the sediment as a layer of uniform conductivity. The quantity $\overline{\boldsymbol{v}}^*$ is the conductivity-weighted vertically-averaged velocity. The assumption of $H/L \ll 1$ means that the horizontal return paths for $\boldsymbol{J}$ are much longer than the vertical paths. Because electrical resistance is proportional to path length, the vertical resistance is negligible compared to the horizontal resistance. This is the physical reason for why oceanic electric fields are vertically uniform.

Electric current density divided by conductivity is the difference between vertically-uniform electric field and that generated by local horizontal water motion, $F_z(\boldsymbol{v}(z) - \overline{\boldsymbol{v}}^*)$. Consider first the case where there is no bottom sediment. If the ocean velocity is entirely depth-uniform, then $\overline{\boldsymbol{v}}^*$ reduces to the vertically-averaged velocity $\overline{\boldsymbol{v}}$. No electric currents flow and the electric potential generated by water motion is exactly balanced by the oceanic electric field at all depths. This situation is analogous to the Hall effect (Halliday et al., 1997), which describes how an electric potential is generated across a conductive strip that moves in a uniform magnetic field.

Electric currents arise when there is sub-bottom sediment or a baroclinic velocity component, for instance if the ocean has a moving surface layer with a motionless deep layer. In the surface layer the velocity is larger than $\overline{\boldsymbol{v}}$, so $\boldsymbol{v} - \overline{\boldsymbol{v}}$ is greater than 0 and $\boldsymbol{J}$ is driven in one direction. The circuit is completed by return electric currents flowing in the opposite direction in the lower layer, where $\boldsymbol{v} - \overline{\boldsymbol{v}}$ is less than 0. Alternatively, the presence of conductive sediment allows electric currents to flow through the sediment, leading to $\overline{\boldsymbol{v}}^* < \overline{\boldsymbol{v}}$.

The parameter $\overline{\boldsymbol{v}}^*$ corresponds physically to the vertically-uniform electric field scaled by F_z. It is linearly related to the vertically-averaged velocity and is reduced by sub-bottom sediment.

The definition of $\overline{\boldsymbol{v}}^*$ (3) can be derived by invoking conservation of charge: the vertical integral of the horizontal electric current density from the bottom of conductive sediment (H_s) to the top of the water column must be zero. Equation (3) can be further simplified by performing a Reynolds decomposition of the water velocity and conductivity in the vertical (where, for the variable c, $\overline{c}$ indicates a vertical average and c' indicates perturbations about the vertical mean). This yields

$$\overline{\boldsymbol{v}}^* = \overline{\boldsymbol{v}}\left(\frac{1+\gamma}{1+\lambda}\right) \quad , \tag{4}$$

where

$$\lambda = \int_{-H_s}^{-H} \sigma \, \mathrm{d}z' \Big/ \int_{-H}^{0} \sigma \, \mathrm{d}z' \tag{5}$$

is the bottom conductance factor, and

$$\gamma = \frac{\overline{\sigma' \boldsymbol{v}}}{\overline{\sigma}\,\overline{\boldsymbol{v}}} \tag{6}$$

is the vertical correlation of conductivity and velocity. The quantity $\overline{\boldsymbol{v}}$ is the depth-averaged velocity.

The amount of shorting through the bottom sediment is described by λ. The form that is consistent with (2) is

$$\lambda = \frac{(H_s - H)\,\sigma_s}{H\,\overline{\sigma}} \quad , \tag{7}$$

which parameterizes the sediment layer as having a uniform conductivity σ_s. Even if the sediment does not have a uniform conductivity, the 1D approximation only responds to the total sediment conductance, the vertical integral of conductance in the sediment that is in the numerator of (5) and (7).

The electrical properties of sediment are in general poorly characterized for calculating λ *a priori*, although they can be estimated on a basin scale as shown in Flosadóttir et al. (1997) or Tyler et al. (1997). The bottom conductance factor can also be incorporated into an effective water depth $D = H(1+\lambda)$ that is the depth of water that has the same vertical conductance as the ocean and sediment column.

The vertical correlation factor $\gamma = \overline{\sigma' \boldsymbol{v}'} / \overline{\sigma}\,\overline{\boldsymbol{v}}$ describes an increase or decrease of $\overline{\boldsymbol{v}}^*$ caused by baroclinic correlations of conductivity and velocity. A layer of fast velocity and increased conductivity drives a larger electric current $\sigma(\boldsymbol{v} \times F_z \hat{\boldsymbol{k}})$ than if the water column were uniformly conductive, which leads to a larger $\overline{\boldsymbol{v}}^*$ for the same $\overline{\boldsymbol{v}}$. Measurements of temperature and salinity simultaneous with electric measurements allow direct calculation of the vertical correlation. Corrections are also possible from hydrographic data or from data archives (Luther and Chave, 1993) by computing representative profiles of geostrophic velocity and electrical conductivity. Previous calculations of γ found it to have less than a 10% influence (Chave and Luther, 1990; Szuts and Sanford, in review, 2011) and to be small outside of strongly baroclinic flows.

Global electromagnetic models often reduce the oceanic layer to a thin shell whose conductance is described by a vertical integral of conductivity, which leads to an alternative definition of $\overline{\boldsymbol{v}}^*$ as the conductivity transport in the ocean divided by the total conductance of the ocean and sediment layers (Tyler et al., 2003). The thin-shell approximation incorporates the one-dimensional nature of oceanic electromagnetic fields, although the quasi-static assumption is not made for the tidal (Tyler et al., 2003) and magnetotelluric (Maus et al., 2007) signals of interest.

3.1.1. Time-varying Ocean Velocity

Until now discussion has focused on quasi-static electric fields that are generated by slowly-changing ocean velocity. For large-scale water motion that changes quickly enough, generally at tidal frequencies or higher, a process called mutual induction couples the ocean across the non-conductive lithosphere with the deep conductive mantle. The time-varying velocities induce electric currents in the mantle, which in turn generate magnetic fields that act to reduce and delay the oceanic electric field. For mutual induction to occur, the velocity field must be horizontally coherent over scales equal to or larger than the depth of the mantle. This conductive layer is below a depth of 500–1000 km, as indicated by interpreted conductivity models (Kuvshinov et al., 2002) and by satellite geomagnetic inversions (Kuvshinov and Olsen, 2006; Maus et al., 2007).

More generally, a scaling analysis of Maxwell's governing equations (Sanford, 1971) showed that the induction parameter $\mu\sigma\omega\mathcal{L}^2$ must be much less than 1 for mutual induction to be negligible (where ω is frequency, $\mathcal{L}$ is a length-scale, μ is magnetic permeability, and σ is electrical conductivity). The appropriate length scales vary from the water depth H to the depth of the conductive mantle. As the induction parameter depends on both time and length scales, this condition is generally satisfied if the phase speed of ocean velocity fluctuations $\omega\mathcal{L}$ is less than 10 m s^{-1} (Tyler et al., 1997). For mutual induction to be small, analysis of an idealized earth geometry constrains large scale flow to have time-scales longer than 12 hours (Sanford, 1971), while realistic profiles of earth conductivity constrain time-scales to be longer than 10 hours for length-scales up to basin size (Chave and Luther, 1990). For instance, intermediate and long-waves in the ocean (including tsunamis) require mutual induction to be included when calculating the electromagnetic fields they generate (Larsen, 1971; Tyler, 2005).

Few observations have been collected that allow a quantitative assessment of the magnitude of mutual induction. Simultaneous $\boldsymbol{E}$ and $\boldsymbol{B}$ measurements (Filloux et al., 1991) have indicated that mutual induction has an upper limit of 30% of the velocity variance at tidal frequencies from data in the open North Pacific during project BEMPEX. That this region of the Pacific is characterized by weak barotropic ocean flow produced by strong and large-scale atmospheric forcing (Chave et al., 1992) suggests that the relative effects of mutual induction might be larger here than in more energetic regimes with smaller length-scales of variability. Comparisons of data collected along the west coast of North America with tidal models find mutual induction effects less than 10% of the barotropic tidal velocity (Filloux et al., 1989: data from EMSLAB compared against the tidal model of Schwiderski, 1979; Althaus et al., 2003: electric field observations compared against the TPXO.3 tidal model of Egbert et al., 1994).

3.1.2. Application to internal waves

Though this treatment focuses on the electromagnetic fields generated by low-frequency ocean circulation, many studies are interested in gravitational internal waves that have relatively fast frequencies (between the buoyancy frequency and f) and horizontal and vertical scales smaller than the water depth. The short vertical and horizontal scales of internal waves preclude magnetic coupling with the deep mantle. A short wave approximation for the oceanic source (Larsen, 1971) yields first-order electromagnetic fields that have no mutual or self-induction, as is readily shown by scaling analysis (Longuet-Higgins et al., 1954; Sanford, 1971). The horizontal electric fields are proportional to the local velocity and are equivalent to the 1D approximation (Larsen, 1971). Similar results are shown for electromagnetic fields generated by baroclinic tidal motion (Preisendorfer et al., 1974).

Compared to mesoscale ocean circulation, baroclinic internal waves differ in that they have no depth-averaged velocity and that their vertical and horizontal scaling is not constrained by the water depth and the length scale of geostrophic motion (the Rossby deformation radius). By considering typical values of the baroclinic Rossby radius and of the Burger number (the ratio between the vertical:horizontal aspect ratio and the eccentricity of ellipse f/N described by geostrophic motion), SzI proposed that the maximum expected aspect ratio for baroclinic motion is $H/L = 0.1$, for which the 1D approximation is accurate within < 1%.

3.2. Higher order terms

The general dependencies of higher order terms can be examined in the analytic forms calculated by Sanford (1971) to motivate what causes perturbations. These terms come from a perturbation analysis where the seafloor varies slowly in height $h(x)$ such that $h/H \ll 1$, and where the horizontal velocity gradients are assumed to be weak $H/L \ll 1$. The results also make use of the same quasi-static assumption used earlier that assumes mutual induction with the conductive deep earth is small.

Sanford (1971) calculates the electromagnetic solution in Fourier space, in which only the lowest-order wave-numbers (or $H/L \ll 1$) are retained in a Taylor expansion. A second order contribution comes from the interaction of the first order solution with a sloping sea surface and the seafloor. The sum of these two solutions gives a closed form solution that is accurate to $(H/L)^2$. Even for situations when a small-gradient assumption is not applicable, the underlying physical basis for higher order terms will remain the same.

Sanford (1971) calculated the full form for horizontal electric current density divided by conductivity to be

$$\frac{\boldsymbol{J}_h}{\sigma} = \overbrace{(\boldsymbol{v}-\overline{\boldsymbol{v}}^*)\times F_z\hat{\boldsymbol{k}}}^{1} + \overbrace{\frac{H(1+\lambda)}{2\pi D}\nabla\times\hat{\boldsymbol{k}}\int_{-\infty}^{\infty}\!\!\int\nabla\cdot F_z\overline{\boldsymbol{v}}^*\,\ln(r)\,dx'\,dy'}^{2} \qquad (8)$$

$$\underbrace{-\nabla_h\left\{\frac{1}{H(1+\lambda)}\int_{-H}^{0}\hat{\boldsymbol{k}}\cdot(\boldsymbol{v}\times\boldsymbol{F})z'\,dz' + \overbrace{\int_{-H}^{z}\hat{\boldsymbol{k}}\cdot(\boldsymbol{v}\times\boldsymbol{F})\,dz'}^{\text{depth-varying}}\right\}}_{3} + O\left(\frac{H^2}{L^2}\right)$$

(depth-varying under term 1)

with

$$r = \sqrt{(x-x')^2+(y-y')^2}$$

$$D = H+\zeta-h+\frac{\sigma_s}{\sigma}(H_s-H+h) \qquad (9)$$

$$\overline{\boldsymbol{v}}^* = \int_{-H+h}^{\zeta}\sigma\boldsymbol{v}\,dz' \Big/ \int_{-H_s}^{\zeta}\sigma\,dz' \,, \qquad (10)$$

where ζ is the surface elevation of the ocean and the other variables are defined earlier. Unlike the discussion of the first order theory, now the variables H and H_s are uniform in space, and thus $h(x)$ and $\zeta(x)$ appear in the definitions for $\overline{\boldsymbol{v}}^*$ and D (above), as well as for λ:

$$\lambda = \frac{(H_s-H+h)\,\sigma_s}{(H+\zeta-h)\,\overline{\sigma}} \quad . \qquad (11)$$

Terms that vary vertically in (8) have been so denoted, and all other terms are vertically uniform.

The first term in (8) is the first-order signal, while the remaining terms (terms 2 and 3) are called higher order terms because they scale as H/L in this formulation.

The second term describes vertically-uniform electric currents that flow in the horizontal plane and that are called poloidal. This mode only exists in situations where there are gradients in the downstream direction and thus is a two-dimensional (2D) horizontal effect. The physical requirement for this term is that the forcing quantity $\nabla \cdot F_z \overline{\boldsymbol{v}}^*$ must be non-zero. The integrand is a convolution of a Green's function ($\ln r$) with a divergence ($\nabla \cdot \overline{\boldsymbol{v}}^* F_z$), and so a delta function forcing yields an integral that decays with $1/r$. Electric currents so generated are called 'non-local' because they are present at locations distant from the generation site.

Divergence of $\overline{\boldsymbol{v}}^*$ can arise either by time-varying ocean currents that cause the sea surface to rise and fall ($\nabla_h \cdot \overline{\boldsymbol{v}} \neq 0$), or by transport across isobaths ($\overline{\boldsymbol{v}}^* \cdot \nabla_h H$) or across gradients in bottom conductance ($\overline{\boldsymbol{v}}^* \cdot \nabla_h \lambda$). To first order because of geostrophy, however, ocean transport is non-divergent and aligned with isobaths, which explains why non-local electrics currents are in general small (Tyler et al., 1997). They have not been investigated in detail, given the high-resolution in both space and time necessary to accurately capture the steep topography and ageostrophic flows that would be most efficient at generating them. Accordingly, they are beyond the scope of the article.

The third term of (8) depends on horizontal gradients of the velocity field and of topography and contains both depth-uniform and depth-varying components. These perturbations are 2D, circulate in the same vertical plane as term 1, and are generated by the horizontal components of the earth's magnetic field. Since the analytic form of term 3 is hard to interpret, results are summarized instead that use full electromagnetic solutions to consider topographic and velocity gradients separately (SzI, SzII), for which perturbations come from both F_z and F_h. Generally, 2D perturbations induced by F_z scale with $(H/L)^2$ and with the normalized topographic height to the power of 1. The associated depth-uniform perturbations depend on λ_{1D} to the power of 1, while the depth-varying perturbations are insensitive to the sediment parameters. Perturbations induced by F_h only depend on H/L to the power of 1 but depend more heavily (a power greater than 1) on the thickness of the velocity feature. At mid-latitudes, F_z-induced perturbations dominate for the depth-uniform component, but the F_h-induced perturbations dominate the depth-varying component.

Since electromagnetic fields are integrative in nature (Luther and Chave, 1993), the signals at one location are spatial averages over some horizontal distance. For the 1D approximation, Chave and Luther (1990) found that this distance is a few times the water depth based on a Green's function formulation of the first-order signal. Because it is essential to include sediment conductance for the first-order response, however, the appropriate vertical scale is the effective water depth D. For 2D perturbations, this averaging length remains remarkably consistent at 1–2 D (SzI, SzII). This makes intuitive sense, for quasi-static electric circuits will have horizontal to vertical aspect ratios that range from very small for the 1D approximation to at most 1 for very strong 2D perturbations. In fact, aspect ratios in the ocean are never expected to reach 1 because of geophysical constraints on water motion (SzI) or on bathymetry (SzII). Accordingly, the limiting scale for averaging will almost always be the vertical scale D.

3.3. Two-dimensional approximation

For analyzing electric signals at Cape Hatteras in section 5, it helps to define in advance a framework for evaluating the full electromagnetic fields calculated later in this article. Because

the analysis is done in a 2D vertical plane, only term 2 of (8) and similar higher order terms that circulate in the vertical plane will contribute to the full solution.

The full electric response can be decomposed into the first-order signal and a 2D perturbations. Physically, $\boldsymbol{E}$ will no longer be vertically uniform and exactly equal to $\overline{\boldsymbol{v}}(1+\gamma)/(1+\lambda)$, while $\boldsymbol{J}/\sigma$ will no longer be exactly proportional to the vertical shear of horizontal velocity. These two parts can be identified in (8): a depth-uniform perturbation is contributed by the first part of the third term, while a depth-varying perturbation is generated by the second part of the third term that involves an integral from $-H$ to z.

Accordingly, the full 2D response is broken into two parts, depth-uniform and depth-varying, that are analogous to the 1D approximation. The first part,

$$\overline{\boldsymbol{v}}^{*}_{2\mathrm{D}} = \frac{1}{F_z H}\int_{-H}^{0} \boldsymbol{E}\times F_z\hat{\boldsymbol{k}}\,\mathrm{d}z \qquad , \tag{12}$$

is calculated from a depth-varying $\boldsymbol{E}$ and may not be the same as the 1D form

$$\overline{\boldsymbol{v}}^{*}_{1\mathrm{D}} \equiv \overline{\boldsymbol{v}}\,\frac{1+\boldsymbol{\gamma}}{1+\lambda_{1\mathrm{D}}} \qquad . \tag{13}$$

For application to non-uniform sediment structure, the 1D form of λ ($\lambda_{1\mathrm{D}}$) has the same general form as (7) except that average conductance and total thickness are replaced by vertical integrals of σ_s in the sediment following (5) and (10).

The second part,

$$\frac{-1}{\sigma F_z}\boldsymbol{J}_h\times\hat{\boldsymbol{k}} \quad , \tag{14}$$

is a depth-varying signal that contains the right hand side of (2) in addition to any other higher order terms. The analogous 1D quantity is $\boldsymbol{v}-\overline{\boldsymbol{v}}^{*}_{1\mathrm{D}}$.

Two-dimensional perturbations are defined as the difference between the 1D and 2D quantities defined above.

4. Field Measurements of Electric Fields

Practically, all instruments that sample electric fields do so with electrodes spaced a fixed distance apart. It is the motion and shape of the instrument platform, however, that determine how the measured potential is related to the *in situ* signal. Most fundamentally, instruments are classified by whether their reference frame is stationary or not.

4.1. Application of the theory to instruments

The first instrument class are fixed in space and have a stationary reference frame. The local velocity ($\boldsymbol{v}\times\boldsymbol{F}$) from (1) cancels the first term of $\boldsymbol{J}_h/\sigma$ in (2), leaving only the electric field generated by $\overline{\boldsymbol{v}}^{*}$. The $\overline{\boldsymbol{v}}^{*}$ signal is easy to interpret for point measurements, but seafloor cables integrate $\overline{\boldsymbol{v}}^{*}$ along their length, and so require more detailed calibration for accurate interpretation (Sanford et al., 1985).

The second class concerns instruments that drift freely at a local and unknown horizontal velocity, and includes both vertical profilers and Lagrangian drifters. An instrument's horizontal motion through the earth's magnetic field induces an additional potential in the electrodes that

cancels the external source $\boldsymbol{v} \times \hat{\boldsymbol{k}} F_z$, leaving an apparent electric field that depends on $F_z(\boldsymbol{v} - \overline{\boldsymbol{v}}^*)$ from (2) (Sanford et al., 1978). The quantity $\boldsymbol{v} - \overline{\boldsymbol{v}}^*$ is a relative velocity profile, and, much like geostrophic velocity calculations, it can be made absolute by reference to any absolute velocity. The difference between the reference velocity and the relative EF-derived velocity is $\overline{\boldsymbol{v}}^*$. Possible sources for reference velocities include shipboard acoustic Doppler current meters (ADCP) (with Expendable Current Profilers (XCPs), Girton et al., 2001), surface GPS fixes (with EM-modified APEX floats, Sanford et al., 2007), subsurface ranging (e.g. electrode-equipped RAFOS floats, Szuts and Sanford, in review, 2011), or instrument-mounted bottom-tracking systems (Absolute Velocity Profile, AVP, see section 5).

If an instrument has an onboard system for obtaining absolute velocity, then the motion of the reference frame can be removed as part of normal processing. Thus, such instruments also indirectly calculate $\overline{\boldsymbol{v}}^*$, the quantity measured by the first class.

The shape of the instrument can potentially distort $\boldsymbol{E}$. A major consideration is the avoidance of conductive metals on the outside of the instrument, as they can generate corrosion currents that obscure the weak oceanic signal. Likewise, ships distort the nearby electric field and so near-surface measurements are best collected 50–100 m away from the vessel — hence the delayed-release collar on XCPs. Long skinny electrode arms (e.g. bottom electrometers) minimally distort $\boldsymbol{E}$, whereas a skinny but non-conductive shell with surface-mounted electrodes, as typical of profiling floats, cause $\boldsymbol{J}$ to flow around the instrument in a predictable manner. The distortion of $\boldsymbol{J}$ is corrected with calibration constants (Sanford et al., 1978).

4.2. Stationary instruments

The use of submarine cables in physical oceanography has a long history, and the cable measurements across the Florida Straits is a well-known example of motional induction measurements. In places where telecommunication cables are not available, point measurements can be obtained with seafloor electrometers (and/or magnetometers). Representative results are summarized from an EM bottom-lander study in the Southern Ocean

4.2.1. Submarine cables

Submarine cables are especially appealing for measuring transport because they respond to spatially-averaged velocities and integrate the electric field (or $\overline{\boldsymbol{v}}^*$) along their length. The Florida Current cable is the best known example and has a time-series that is nearly 30 years long. It has been discussed in detail by many articles (Larsen and Sanford, 1985; Spain and Sanford, 1987; Larsen, 1992), and is now an essential component for closing the mass transport of the Atlantic meridional overturning circulation (Cunningham et al., 2007).

Aside from the broad availability of retired or in-use submarine cables (Nilsson et al., 2007; You, 2010), a commercial version of a bottom electrometer called HPIES (Horizontal electric field and Pressure-equipped IES, Sanford, pers. comm.) is under development. It combines the three spatially-integrating quantities of electric field, bottom pressure, and IES travel-time (Luther and Chave, 1993) and can readily be connected to cabled observing systems or can be used to form a 'synthetic' submarine cable when deployed in a transect. Also, increased efforts to provide transport monitoring with submarine cables (You, 2010) require a careful application of theoretical and practical knowledge gained since the start of the Florida Strait monitoring effort, including independent calibration procedures.

4.2.2. Seafloor electrodes

The BEMPEX project (Luther et al., 1991) used bottom electrometers and magnetometers to study electrical signals in the deep central North Pacific over a wide band of subtidal and supertidal frequencies. The EF-derived subtidal water velocity was compared to current meter measurements, and the supertidal signals were compared to earth conductivity profiles in combination with magnetic observations. The depth-uniform subtidal velocity from the electrometers responded better to the weak signals in the central North Pacific than did the 3–4 rotor current meters, which frequently stalled and under-resolved the vertically-averaged velocity.

For the Sub-Antarctic Flux and Dynamics Experiments, Meinen et al. (2003) [1] used electrometers in the Southern Ocean to obtain absolute velocity profiles from a combination of bottom electrometers and inverted echo sounders (IES). The baroclinic structure of the Antarctic Circumpolar Current (ACC) was obtained from a gravest empirical mode (GEM) analysis of the IES travel time measurements, and $\overline{\boldsymbol{v}}$ calculated from the electrodes served as a spatially-averaged reference velocity. This approach explicitly resolved the absolute velocity field of the ACC, unlike earlier hydrographic studies that assumed a level-of-no-motion at the seafloor, in order to fully characterize the momentum and energy budgets. Though the time-averaged bottom velocity (Figure 1a,b) was small, it fluctuated over a range of 0.3 m s^{-1}. The large velocity fluctuations below 1500 m in stream coordinates (Figure 1c-f), equal to or larger than the time-averaged velocity, highlights the importance of full-depth eddies in the Southern Ocean.

4.3. Lagrangian or profiling instruments

The first generation of profiling instruments was developed around 1980 for recoverable (Sanford et al., 1978) and expendable probes (Expendable Current Profiler (XCP), Sanford et al., 1982) that obtain vertical profiles of relative velocity. Sanford et al. (1985) further developed a more complex profiler, the Absolute Velocity Profiler (AVP), to include absolute velocity measurements for reference purposes as well as payload for other sensors (optical backscatter, Stahr and Sanford, 1999; dissipation, Winkel et al., 2002, Lee et al., 2006). Electrodes have also been added to other microstructure profilers (the Multi-Scale Profiler, Winkel et al., 1996; the High Resolution Profiler II, K. Polzin, pers. comm., 2008). A commercial APEX float with an electromagnetic subsystem called an EM-APEX (Sanford et al., 2007, 2011) has been used in multiple field campaigns around the world.

Profiling floats are especially suited for electric field measurements because of their autonomous nature and the low power requirements of electrodes. Smaller versions such as the XCP or the EM-APEX are the only current profilers suitable for deployment by aircraft and can also be deployed from ships under harsh conditions. This allows for quick deployments or surveys, such as for surveying quickly-evolving ocean process under rough weather (Girton et al., 2001), or in front of an advancing hurricane (D'Asaro et al., 2007). Larger instruments can carry additional sensors, while freely drifting instruments act as distributed sensors that do not require ship-based support (Gille et al., 2007). Instruments such as EM-modified RAFOS floats (Szuts, 2004) or EM-APEX are some of the few Lagrangian instruments that, aside from their drift paths, measure velocity over long deployments.

4.3.1. XCP Survey in Denmark Strait

The Denmark Strait is one of the locations along the Greenland-Scotland ridge over which dense water flows from the Norwegian Seas into the Atlantic as part of the Atlantic meridional

[1] more info at `http://www.soest.hawaii.edu/oceanography/dluther/SAFDE`

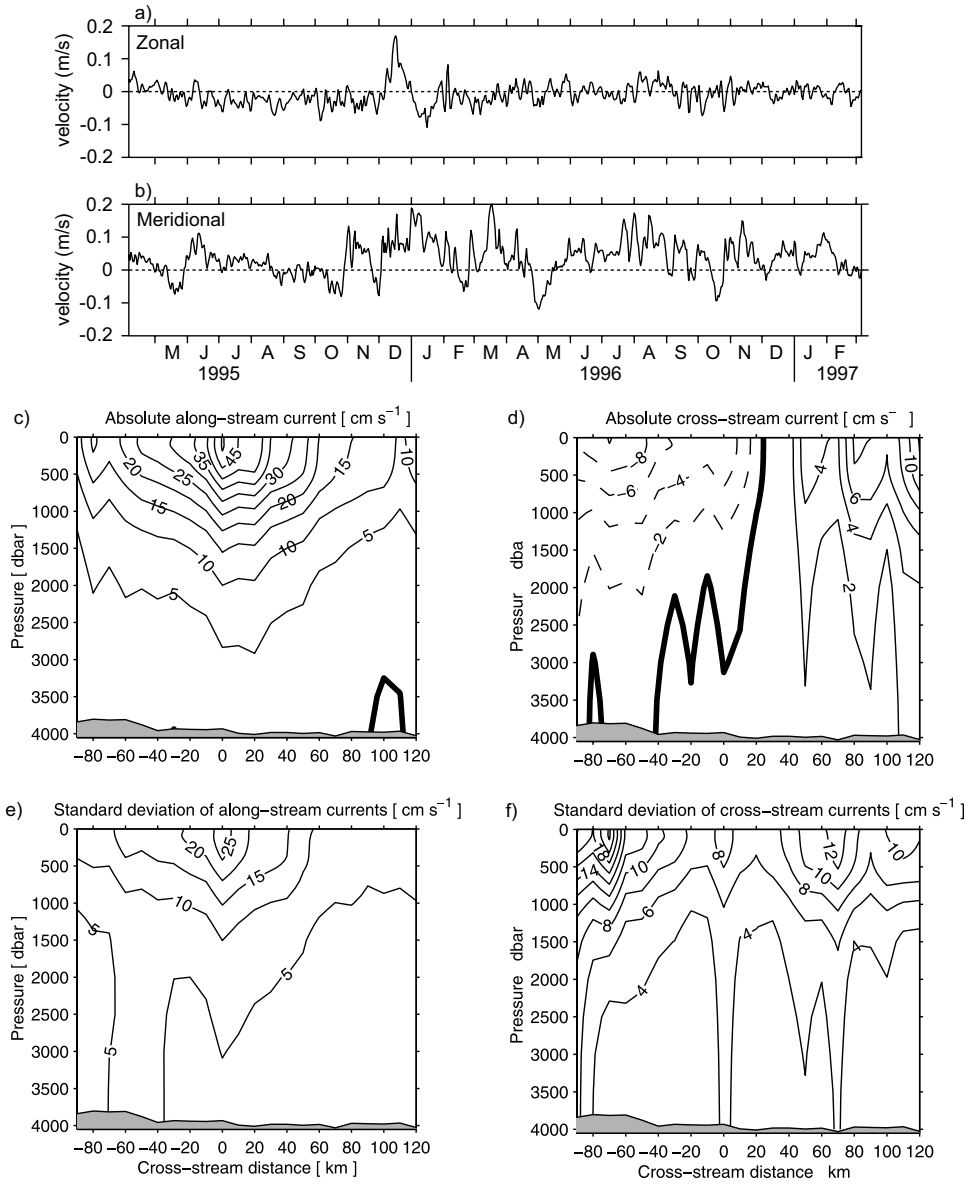

Figure 1: Results from the Sub-Antarctic Flux and Dynamics Experiment (Meinen et al., 2003) showing absolute velocity fields obtained by combining an IES-based GEM technique with bottom horizontal electric field recorders (Meinen et al., 2003): a) zonal and b) meridional absolute velocities at 3500 db at the site of HEFR 10 (water depth of ~4268 m), and a stream coordinate analysis of c) mean along-stream velocity, d) mean cross-stream velocity, e) standard deviation of along-stream velocity, and f) standard deviation of cross-stream velocity. The mean topography in stream coordinates is shown in c)–f), but the actual bottom topography is rougher. (modified versions of Figures 2, 4 and 5 from Meinen et al., 2003)

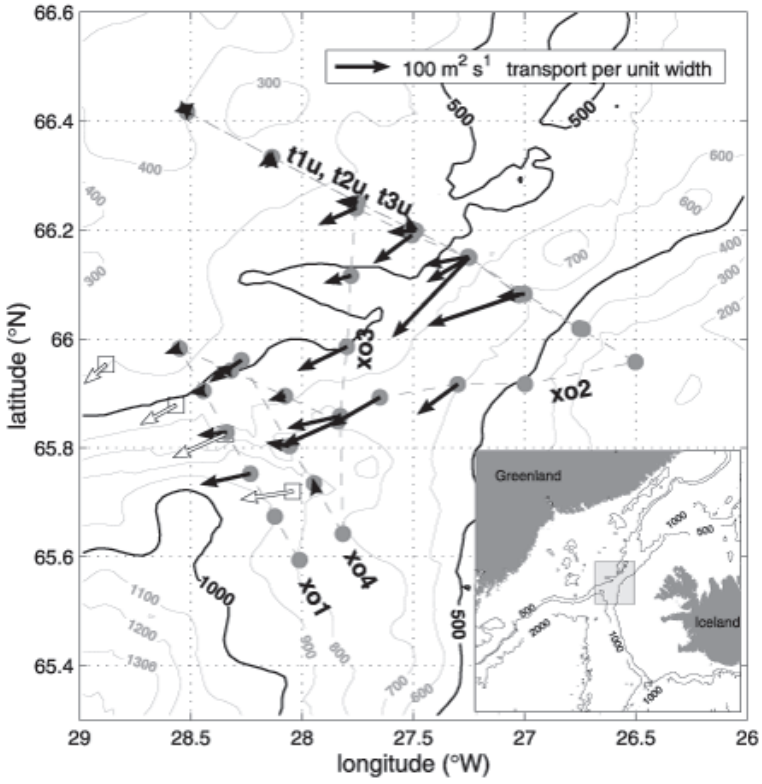

Figure 2: Cold water transport in the Denmark Strait (from Girton et al., 2001, their Figure 1). Five-week averaged transports at XCP stations (dots) are shown by solid arrows for dense water transport ($\sigma_\theta > 27.8$). Transport from current meters (open squares) are shown by open arrows for cold water transport ($\theta < 2$° C) from data collected as part of the ICES "OVERFLOW '73" experiment (Ross, 1984).

overturning circulation. Although this region is one of the choke-points for overflows, stormy weather and strong and episodic events create observational challenges.

During a cruise in the early 2000s, despite frequent storms that prevented over-the-side sampling, multiple cross-sections of the region were obtained with XCPs. The fast 2–5 day timescale of the region further required rapid sampling to minimize aliasing biases (Figure 2). A summary figure from Girton et al. (2001) (Figure 2) shows the transport of dense water from their observations. A statistical comparison between the 7 XCP sections and a current meter array 25 years earlier (Ross, 1984) shows no statistically significant difference in transport between the two sets of observations.

4.3.2. EM-APEX in Hurricane Frances

The EM-APEX provides velocity capabilities to a float that is part of the global ARGO network. Its user-specified sampling plan ranges from the standard ARGO plan of 10-day drifts between profiling and surfacing to continuous profiling for resolving fast kinematic processes. One recent program investigated the upper-ocean response to strong wind forcing caused by a

hurricane (Figure 3). Strong surface mixing and the input of kinetic energy deepen the thermocline, excite horizontal inertial oscillations related to the cold wake (D'Asaro et al., 2007), and generate internal waves that propagate downward away from the surface layer. These observations serve as an important constraint on air-sea interactions at high wind speeds (Zedler et al., 2009).

Other uses of EM-APEXs extend sampling in space or time around or between detailed ship-based surveys. Scientific questions addressed include formation of subtropical mode waters (Climode Group, 2009), diapycnal and isopycnal mixing of waters in the ACC (Gille et al., 2007), or topography-induced mixing in the ACC at the Kerguelen Plateau (H. Phillips, pers. comm. 2010).

4.4. Factors to consider for field programs

The following factors need to be considered for accurate observational work. The exact importance of each is determined by the quantity measured, whether the absolute $\boldsymbol{E}$ or the vertical profile of $\boldsymbol{J}(z)/\sigma(z)$, and the geographic setting of the study site. As an aid, however, the factors are roughly ordered by magnitude (shown in parentheses) and should be compared with magnitudes for oceanic signals of 1–100 μV m^{-1} corresponding to velocities of 0.01–1.0 m s^{-1} at mid-latitudes.

- Electrode self-potential (order 1 mVm^{-1}). Self-contained instruments are designed to measure and remove these signals, because electrode self-potentials, though varying slowly due to environmental changes, are 1000 times larger than those of oceanic signals. The electrodes themselves are typically well-protected to minimize sudden environmental changes due to temperature or salinity/chemistry variations. Practically, the self-potentials are measured and removed by switching the electrode orientation, either by instrument rotation or by periodic switching of electrical contacts. When this is not possible, such as for submarine cables, calibration is necessary to determine the self-potential heuristically (Larsen, 1992). Silver-silver chloride electrodes have been used most extensively because of their accuracy (Sanford et al., 1982), but other types have been investigated (Crona et al., 2001).

- Sediment conductance for interpreting $\overline{\boldsymbol{v}}^*$ (as low as 0–10% of $\overline{\boldsymbol{v}}$ in thinly sedimented regions, up to 50–100% of $\overline{\boldsymbol{v}}$ in heavily-sedimented continental slopes, and potentially more in shallow continental shelves). Approximate values can be obtained from maps of sediment thickness (Tucholke, 1986; Laske and Masters, 1997), yielding estimates of λ within 10–50% (as done in Flosadóttir et al., 1997). More detailed geologic data can also be consulted (section 5.1) to incorporate stratigraphic and lithologic knowledge. Alternatively, this factor can be determines by repeat observations of $\overline{\boldsymbol{v}}^*$ and absolute $\overline{\boldsymbol{v}}$ (see section 5.2). This factor is only important for interpreting $\overline{\boldsymbol{v}}^*$ and does not affect profiles of $\boldsymbol{v}(z) - \overline{\boldsymbol{v}}^*$.

- Earth's magnetic field (a few percent). Recent field models of the earth's core field are accurate to 10 nT (International Geomagnetic Reference Field 10 (IGRF10), Maus et al., 2005). Local crustal anomalies can be up to 1000 nT (Korhonen et al., 2007) at scales smaller than the 4000 km resolution of Maus et al. (2005), which is a few percent change of the mean strength of the magnetic field.

- Magnetotelluric activity (magnitude highly dependent on sampling method and study location). Magnetic storms are globally coherent and strongest at high latitudes and contain high frequency signals, while smooth daily fluctuations (called quiet day signals) are found

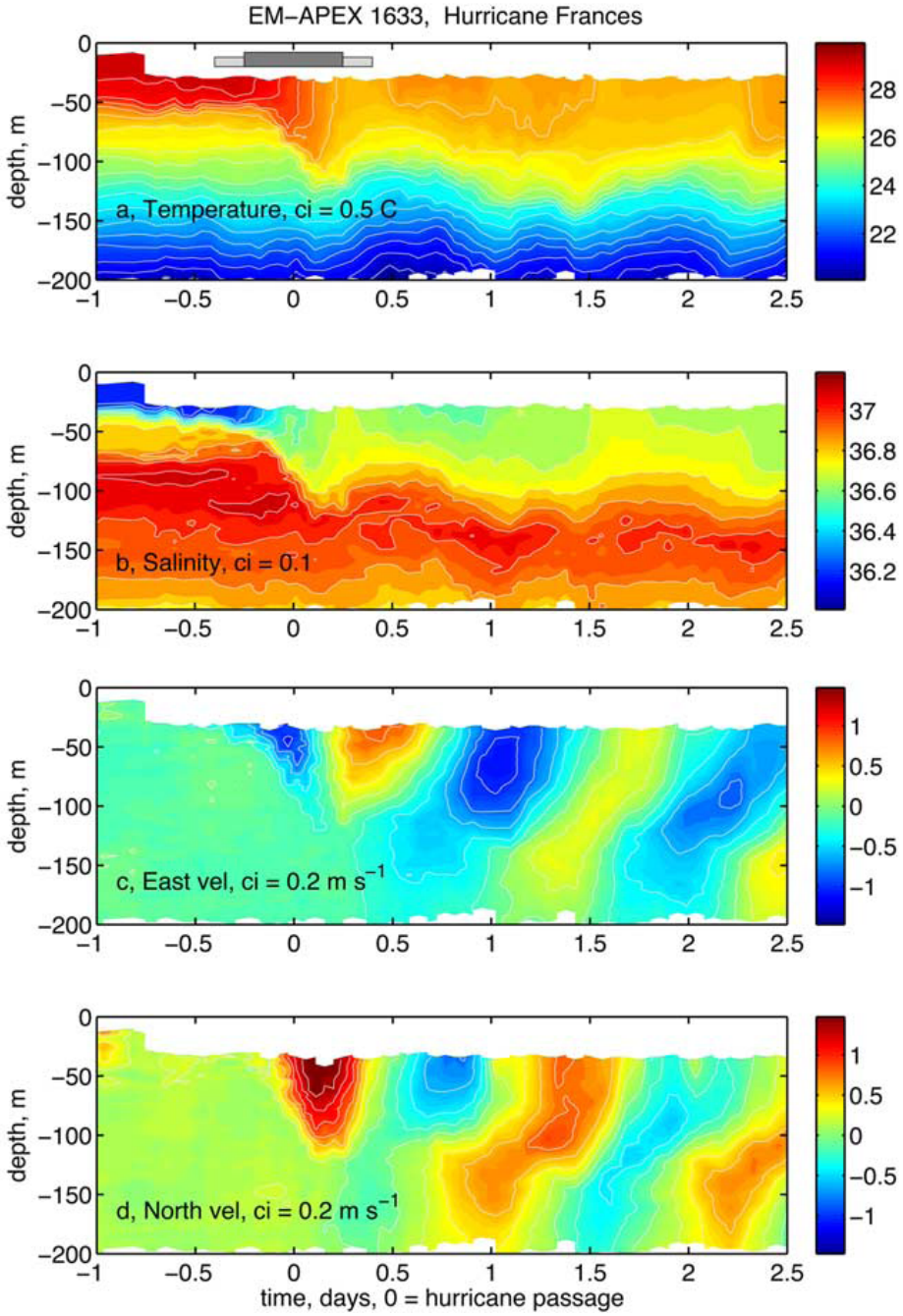

Figure 3: Observations from an EM-APEX sampling under a hurricane (from Sanford et al., 2007, their Figure 1): time-evolution of a) temperature, b) salinity, c) east velocity, and d) north velocity. The instrument is located 55 km to the right of the hurricane track, close to the radius of maximum winds, and the time of strong wind forcing is shown by the bar in a) for two threshold values. For this and all subsequent captions that refer to color, see the online version for color graphics.

at all latitudes. These signals can be removed from time-series by transfer functions relative to a remote reference site (Simpson and Bahr, 2005). Global magnetotelluric activity is summarized by the Kp-index, which is obtainable from the National Oceanic and Atmospheric Administration (NOAA) National Geophysical Data Center for historical data and from the NOAA Space Weather Prediction Center for current conditions and forecasts. Ionospheric signals in the ocean are most significant at periods less than one day (Luther et al., 1991; Chave et al., 2004) and are stronger near the (magnetic) poles than the equator. The integral nature of cable measurements results in longer submarine cables responding more strongly to global-scale magnetotelluric fluctuations than to shorter-scale oceanic fluctuations. Magnetotelluric signals can be removed by transfer functions (Larsen, 1992; Chave et al., 2004) or by filtering (Meinen et al., 2010). For reference, bottom electrometers at 50°S showed a standard deviation in the 2.5–3.8 hour band (Chave et al., 2004) that has equivalent velocities of 0.02–0.03 m s^{-1}. For the Florida cable, the standard deviation from ionospheric signals at periods less than 3 days is the same order as the oceanic signal, because, despite the low latitude, the cable responds strongly to large-scale quiet day fluctuations (Larsen, 1992).

- Topography that is rough over scales smaller than the inherent EM horizontal averaging scale of the ocean (depends on conductivity contrast and spatial scales of roughness). Rough and non-conductive bathymetry, such as craggy basalt characteristic of mid-ocean ridges, may distort electromagnetic fields close to the seafloor. These frequency-independent galvanic distortions, which have been observed in unsedimented regions of rough topography, can be removed by transfer function methods (Chave et al., 2004).

- Quality of the reference velocity (typically 0.01–0.05 m s^{-1}). The total error of referenced EM-derived velocity profiles is the sum in quadrature of the reference velocity and that of the EM-measurements.

- Other external electromagnetic fields, such as man-made signals in coastal zones (typically of high frequency, such as 60 Hz contamination) or weak fields associated with the global electric circuit (Markson, 2007). The global electric circuit is driven by an uneven distribution of atmospheric lightning over the globe (Tinsely et al., 2007). Though on average the resulting electric currents are very weak, they may be concentrated in the Strait of Gibraltar or other straits that connects large isolated seas to the deep ocean basins (Johnson et al., 1994; Tyler et al., 1997).

5. Case Study at Cape Hatteras

To investigate the limits of the 1D theory, Sanford et al. (1996) collected EF measurements at Cape Hatteras, a location that breaks many of the assumptions of the 1D approximation. The complexities at this location include a steep continental slope, a fast Gulf Stream with a sharp northern edge, and thick and inhomogeneous sediment layers. The rest of this article investigates the signals measured at this location to quantify their influence on electromagnetic fields.

5.1. Observational data

During R/V *Endeavor* cruise 239, a transect SE of Cape Hatteras (Figure 4) was occupied for 6 days in July, 1992 (Sanford et al., 1996). Thirty full water column profiles of electric field and

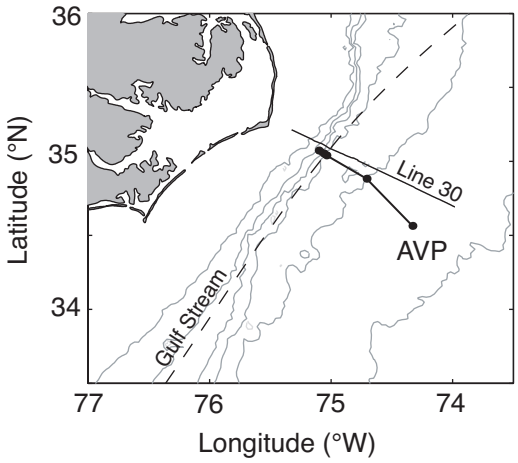

Figure 4: Chart showing the study area at Cape Hatteras: AVP stations (black dots), AVP transect (thick solid black line), the Line 30 seismic transect (Hutchinson et al., 1995), and a schematic path of the Gulf Stream (Savidge, 2004). Isobaths are shown at 100, 500, 1000, 2000, 3000, and 4000 m.

hydrographic quantities were collected with the Absolute Velocity Profiler (AVP) at 5 stations (Szuts, 2008). Three inshore stations at isobaths of 500, 1000, and 2000 m were repeated 6–7 times each, and two deeper stations at isobaths of 3000 and 3500 m isobaths were repeated 2–3 times each. The shallow stations are close together (within 3–5 km) because of the steepness of the continental slope, while the deeper stations are further apart (within 30–50 km).

The AVP is a free falling vertical profiler that rotates as it descends and ascends. Two pairs of electrodes and an internal magnetometer measure the ambient electric and magnetic fields, and the rotation modulates the oceanic signal for separation from the electrode self-potentials. An onboard acoustic Doppler system measures the instrument's absolute velocity when it is within 50–250 m of the seafloor. Weights suspended below the instrument cause it to fall at 1 m s^{-1} and are released mechanically when they hit the bottom, after which the instrument returns to the surface at a similar speed. Additional sensors include a CTD package and shear probes. The instrument is fully described in Sanford et al. (1985).

The electrodes measure an apparent electric field that is equivalent to $\boldsymbol{J}_h/\sigma$ in (2), given the tall and narrow shape of the instrument (Sanford et al., 1978). The absolute Doppler velocities serve as reference velocities and allow the absolute velocity profile $\boldsymbol{v}(z)$ and $\overline{\boldsymbol{v}}^*$ to be calculated. The processed absolute velocities are calculated with a vertical resolution of 4 m and have instrumental accuracy of 0.01-0.02 m s^{-1} (Sanford et al., 1985).

For interpreting the measured electric fields, it is also necessary to characterize the geometry and electrical properties of sediment layers from geophysical observations. The layer geometry comes from a nearby seismic transect (Line 30, Hutchinson et al., 1995), while the electrical properties come from *in situ* resistivity measurements made in selected bore holes along the continental margin (for data sources see Szuts, 2008). The bore holes, or wells, are translated to the seismic line by placing them at the same isobath. This approach assumes that along-margin depositional histories are uniform between the bore-holes and the seismic line, and thus that sediment properties are also similar. The full sediment column underneath the continental shelf is well constrained by deep wells, but there are few wells on the continental rise that extend close

to the rocky basement. Sediment types are compiled for three depositional environments, with well-defined shelf and deep-water environments connected by a transitional slope environment. Layers in the borehole are matched to layers in the seismic transect by age, and then the average electrical conductivity from the well layer is transfered to the seismic layer (Szuts, 2008). Care is taken that the lithology of the seismic layer matches that in the sediment core. Multiple wells are considered to obtain robust results.

5.2. 1D analysis

Following standard processing, the 1D approximation is used to calculate velocities from the measured electric fields. This assumption is verified later. The electric fields are demodulated, rotated from magnetic to geographic coordinates, and converted to a relative velocity profile following

$$\boldsymbol{E}_{\text{measured}} = \boldsymbol{v}_{\text{EF}} \times \hat{\boldsymbol{k}} F_z = (\boldsymbol{v} - \overline{\boldsymbol{v}}^*) \times \hat{\boldsymbol{k}} F_z \qquad . \tag{15}$$

Over the depth range when the acoustic Doppler velocimeter makes measurements, $\overline{\boldsymbol{v}}^*$ is calculated as the average offset between the apparent velocity ($\boldsymbol{v}_{\text{EF}}$) and the absolute Doppler velocity. This quantity is used to make the velocity profile absolute. Magnetic field values are calculated from the IGRF10 field model (Maus et al., 2005).

The velocities are rotated into stream coordinates such that $\hat{\boldsymbol{y}}$ and v are directed downstream and $\hat{\boldsymbol{x}}$ and u are directed offshore. The vertical correlation factor $\boldsymbol{\gamma}$ is calculated from $\boldsymbol{v}_{\text{EF}}$ and CTD conductivity. The rotation angle to convert to stream coordinates is calculated as the inverse tangent of $\gamma_{u_g}/\gamma_{v_g}$, where γ is calculated from (6) for velocities in geographic coordinates that are directed east (u_g) and north (y_g). This criterion yields angles (Table B.2 in Szuts, 2008) that are within a few degrees of the direction of vertically-integrated velocity.

To evaluate the 1D approximation I evaluate the accuracy of (4), in which the only unmeasured quantity, the bottom conductance factor λ, acts as the slope between $\overline{v}(1+\gamma)$ and $\overline{v}^*$. If the 1D theory is accurate, all profiles should define a linear slope that goes through the origin. A necessary prerequisite for this approach is the fact that $\overline{\boldsymbol{v}}$ changes in magnitude at successive repeat profiles.

With relatively small sample sizes at each station, care must be taken in the error analysis. Although there are two profiles for each deployment (a downcast and an upcast), the integral time-scales for the low-frequency ocean-generated signals are longer than the average time separating up- and down-casts. Using a method to calculate the additional degrees of freedom from the upcast that is based on the correlation of $\overline{\boldsymbol{v}}$ and $\overline{\boldsymbol{v}}^*$ between profiles (Bretherton et al., 1999) only yields 0.1 additional degrees of freedom at the 1000-m and 2000-m stations (Szuts, 2008). Two profiles were removed from the 500 m station (drops 414 and 427) because they were collected at water depths significantly different from the other drops at that station.

At all stations, $\overline{\boldsymbol{v}}(1+\gamma)$ and $\overline{\boldsymbol{v}}^*$ fall along well defined lines (Figure 5) that capture more than 99% of the variance (Table 1). The 1000-m and 2000-m stations agree with the 1D approximation because, respectively, their intercepts are either indistinguishable from 0 or are the same size as instrumental precision. Unfortunately, the small degrees of freedom at the 3000 and 3500 m stations prevents further analysis of them.

The 500-m station, however, has a non-zero y-intercept despite the high linearity of the fit. Although a fit at the 500-m station that is forced to go through the origin would still recover most of the covariance, showing the predominance of the 1D signal, this indication of higher order effects serves as a starting point for evaluating and quantifying what processes are responsible.

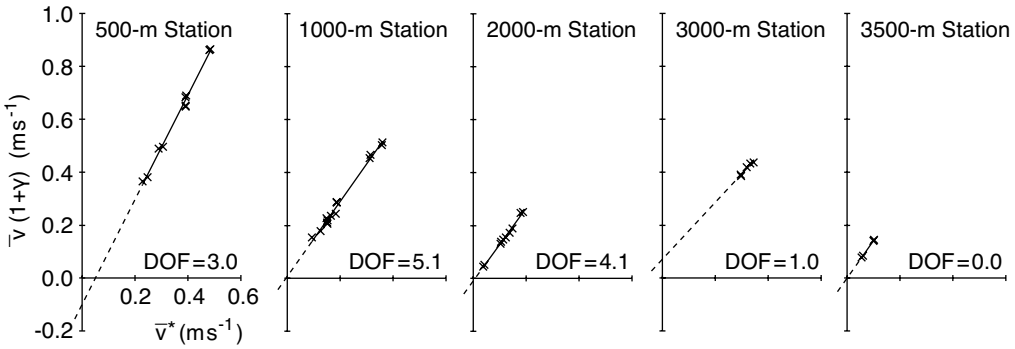

Figure 5: AVP observations of $\overline{v}^*$ and $\overline{v}(1+\gamma)$ (crosses) with the fit at each station (solid, extrapolation is dashed).

Table 1: Linear fits to the AVP data at each station following shown in Figure 5. N is number of profiles, DOF is the degrees of freedom in a linear fit, the linear fits have slopes given by $1+\lambda$ and a y-intercept y_0, and the confidence limits on λ and y_0 are standard errors.

station	N	DOF	λ	y_0 (m s^{-1})	r^2
500	10	3.0	0.97 ± 0.06	-0.10 ± 0.02	0.996
1000	14	5.1	0.42 ± 0.04	0.007 ± 0.010	0.995
2000	12	4.1	0.37 ± 0.04	-0.010 ± 0.005	0.996
3000	5	1	0.08 ± 0.14	0.071 ± 0.0009	0.976
3500	4	0	0.42 ± N/A	0.0009 ± N/A	N/A

5.3. Modeling the Cape Hatteras region

Higher horizontal resolution than resolved by the observations is necessary for a detailed interpretation of higher order terms in motional induction. This resolution is provided by applying an electromagnetic numerical model to this location.

5.3.1. Model for Ocean Electrodynamics (MOED)

The full-complexity electromagnetic response at Cape Hatteras is solved with an electromagnetic numerical model called the Model for Ocean Electrodynamics (MOED, Tyler et al., 2004). MOED is a 3D, conservative, finite-difference model that solves Maxwell's equations in the frequency domain for electric and magnetic gauge potentials, given prescribed conductivity and velocity fields. Validation of this model is demonstrated in Tyler et al. (2004) for 1D, 2D and 3D cases that have analytical solutions, while the 2D and zero-frequency implementation used here is validated against a numerically-evaluated analytical solution in SzI.

An accurate quasi-static electromagnetic solution requires a detailed and accurate initialization for the local environment: the oceanic velocity and electrical conductivity come from the AVP observations, while the sediment geometry and electrical conductivity come from a synthesis of local geophysical data (Figure 6).

The prescribed oceanic properties come from the station-averaged profiles of water conductivity and velocity measured by the AVP. The down-stream velocities and conductivities in the water are based on the station-averaged vertical profiles collected by the AVP, gridded to the model grid with a cubic scheme that makes first and second derivatives continuous. The Gulf Stream is not expected to extend onto the continental shelf past the shelfbreak (at a depth of 100

m), so the inshore limit of the Gulf Stream is set at the 250 m isobath (x = 2 km). The offshore extent is chosen at x = 150 km. The horizontal velocity structure is only constrained at 7 locations: the 5 AVP stations and the two bounding locations. While the offshore extent of the Gulf Stream is well-constrained by many studies, its extent inshore of the 500-m isobath is not known at Cape Hatteras.

The model grid needs to have short spatial resolution but a small enough number of grid points to be computationally solvable. This was met with a grid that has highest resolution over the continental slope (Δx = 50 m for $0 < x < 20$ km) and upper water column (Δz = 10 m above $z = -3000m$), beyond which the grid spacing increases by 5% up to a maximum spacing (Δx = 200 m, Δz = 40 m). The vertical resolution is 5 m in the upper 100 m in order to resolve the continental shelf and smoothly increases to 10 m below $z = -100$ m.

The sloping conductivity interfaces in the model domain need to be smoothed for numerical stability. For the water/sediment and sediment/crust interfaces the conductivity over 4 grid-points in the vertical was smoothed based on the exact interface depth according to

$$\sigma(z_i) = \frac{1}{2}\left[1 + \sin\left(\frac{2\pi(z_i - z_{\text{interface}})}{4\Delta z}\right)\right]\left(\sigma_{\text{upper}} - \sigma_{\text{lower}}\right) + \sigma_{\text{lower}} \quad , \tag{16}$$

where the points z_i are within 2 grid points of the depth of the interface $z_{\text{interface}}$, Δz is the vertical grid-spacing, and σ_{upper} and σ_{lower} are the conductivities of the upper and lower layers. A non-conductive crust underlies the sediment. Realistically, oceanic crust has conductivities of 0.0001 – 0.03 S m^{-1} (Chave et al., 1992; Simpson and Bahr, 2005), which is at least an order of magnitude smaller than sediment conductivity and will not support a significant flow of electric current. Finally, both velocity and electrical conductivity are smoothed in a vertical plane with a Gaussian filter that is 3 points wide in the horizontal and 5 points wide in the vertical.

The importance of the water depth for defining theoretically-derived vertical integrals requires that the measured bathymetries in the AVP observations and in the geologic data be made consistent in a careful manner. Because the velocity is only constrained at 5 stations, a bottom topography that varies over smaller scales will be inherently inconsistent. Further motivation for smoothing topography is that previous studies (Chave and Luther, 1990; SzII) show that the 1D signal is averaged over horizontal distances 1–2 times the effective water depth. For these reasons a smoothed topography is used instead of that present in the seismic lines or that underneath the AVP transect. The raw topography database (Smith and Sandwell, 1997) is filtered with a 9-km wide 2D Gaussian smoothing kernel, and the dominant scales of topography along the transect are further extracted by fitting isobaths to quadratic functions in horizontal space.

The direction of the Gulf Stream axis (toward 48° True) contains a significant component perpendicular to geomagnetic north, so the horizontal magnetic field contributes to the full solution. The magnetic field values used (IGRF-10) are $F_z = -46,860$ and $F_h = 22,290$ nT, with a magnetic declination of -10.2° True. The cross-product of $\boldsymbol{v}$ and $\boldsymbol{F}_h$ is 85% of its maximum value, showing that this location is suitable for quantifying perturbations induced by $\boldsymbol{F}_h$. During the sampling the magnetic storm index K_p was low, and a more detailed investigation (Szuts, 2008) of ionospheric-induced signals and their potential amplification due to the coastline, the so-called coast effect, found no correlation between modeled magnetotelluric signals and residuals of $\bar{\boldsymbol{v}}^*$ relative to the 1D fit.

5.3.2. Sediment conductivity structure

The final conductivity structure from the geophysical and AVP data, as gridded onto the model domain, is shown in Figure 6. The deep sediment is compact and only weakly conductive

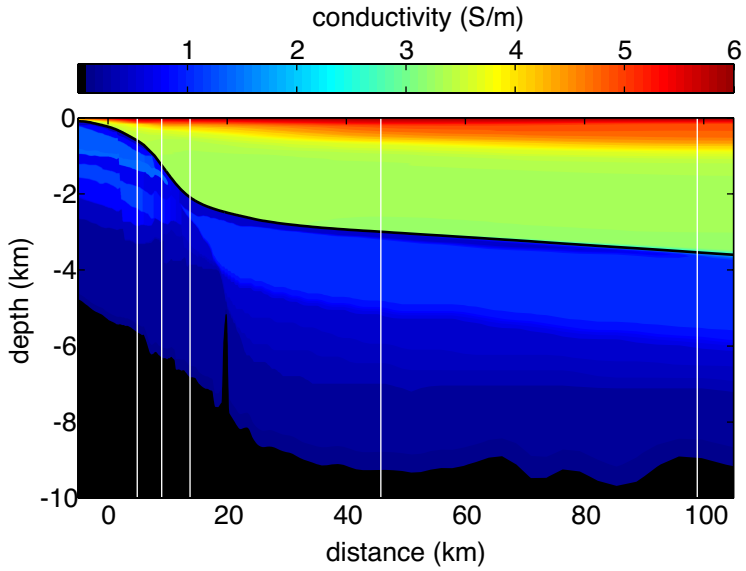

Figure 6: Conductivity input into MOED (color), based on station-averaged conductivity profiles and compiled geophysical data. The locations of the stations are shown by white lines, a relatively non-conductive diapir is seen near 20 km, and non-conductive basement is underneath the sediment layers (depths of 5–10 km).

(0.2–0.3 S/m), while shallower sediment is more porous and thus more conductive (1–1.5 S/m).

It is worth highlighting geological features near Cape Hatteras for comparison with other locations. Sediment is unusually deep because of a deep trough in the oceanic crust. The bathymetry at Cape Hatteras is especially steep, with maximum slopes of 12–16° and a bimodal distribution centered at 4.5° and 10° (from topography by Smith and Sandwell, 1997; Popenoe, 1985). This part of the continental slope has eroded 10–20 km since the early Miocene because of scouring by the Deep Western Boundary Current (Popenoe, 1985). This history means that the slope only has a thin layer of unconsolidated and relatively conductive sediment compared to the shelf, and that near-surface sediments on the slope are likely more solidified and less conductive than suggested by their current depth in the sediment column.

Two additional geologic features can appreciably reduce sediment conductivity: salt diapirs and gas hydrates. Both disrupt the typical structure of oceanic sediment — mineral grains with salt water filling the surrounding pores — by replacing the pore fluid with less conductive material. Salt diapirs are caused by ancient salt deposits being squeezed out of their original beds by subsequent sediment loading to form vertical plumes of salt. Diapirs form a line along the 3000 m isobath south of Cape Hatteras, have diameters less than 25 km, and typically do not reach the top of the sediment column. Although a diapir is present in the Line 30 seismic transect near $x = 20$ km, unfortunately only 2 AVP profiles at the 3000-m station do not give enough statistical confidence to evaluate how the diapir affects oceanic electric fields. Gas hydrates are ice-like complexes of gases and water that form in sediment under high pressure and cold temperatures, and are generally found within the upper 1000 m of the sediment column (Ellis et al., 2008). Near Cape Hatteras, survey results (Dillon et al., 1994) indicate no hydrates in water shallower than 3000 m.

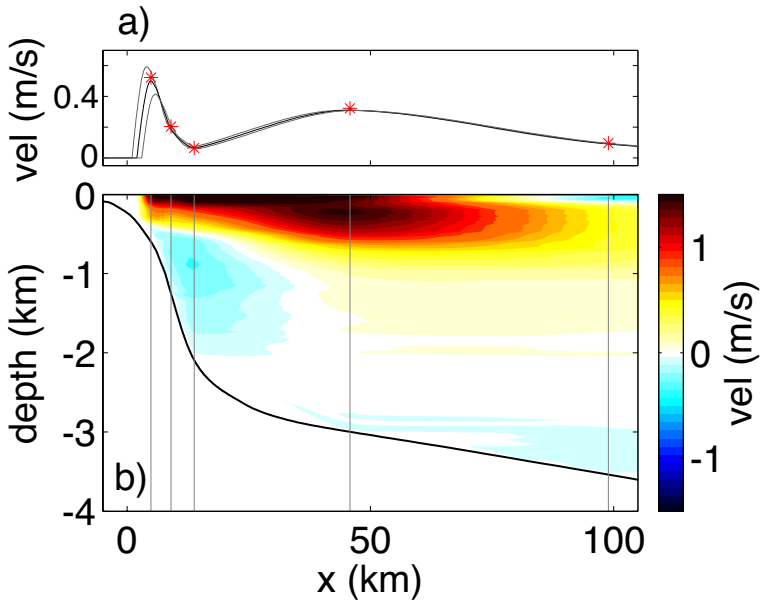

Figure 7: Velocity input into MOED. (a) The depth-averaged velocity $\overline{v}$ used in the model (black), and when shifted by ±1 km to either side (gray, see section 5.4.2), with the AVP-calculated $\overline{v}$ (∗). (b) The gridded velocity (color) based on the 5 station-averaged velocity profiles (vertical black lines). See text for details.

5.3.3. MOED results

Based on the input velocity and conductivity fields, the model calculates the corresponding electromagnetic fields in the 2D transect. The model is forced with time-averaged velocity profile at each station, so the results are initially interpreted in a time-averaged sense.

The prescribed velocity is shown in Figure 7 for the downstream velocity component. By definition the model $\overline{v}$ (solid black line) fits the AVP data (*) at the 5 stations (top panel). Outside of the first and last stations, the velocity goes to 0 at predefined locations to yield a bounded Gulf Stream, while a cubic interpolation technique maintains a continuous second derivative between stations. The station-averaged velocities show a maximum $\overline{v}$ at the 500 m isobath, and, though the 1000 and 2000 m isobath stations resolve the seaward structure of this maximum, the landward structure remains unresolved. On the upper continental slope the velocity changes on horizontal scales of $L = 5$ km. Despite the offshore stations being widely spaced, I assume that horizontal scales are much larger there than over the continental slope. This presumption is substantiated by many studies that characterize the cross-section of the Gulf Stream close to its main axis (Watts et al., 1995). The depth of the Gulf Stream, defined as the depth where the velocity direction changes compared to the surface waters, is 400–500 m along the continental slope and deepens to 1000 m over the continental rise.

Definitions for two-dimensional perturbations have been introduced earlier in equations (12) to (14). To maintain consistency with the numerical model results, the 1D sediment factor λ_{1D} is calculated from the sediment conductivity distribution used by the model.

The choice to initialize the model with velocities from a 1D interpretation of the measured electric fields may appear at odds with calculating 2D effects. I proceed assuming that 2D ef-

fects are small but will verify this later in section 5.4.3. This approach amounts to a numerical perturbation analysis, in which the velocities first used to initialize the model can be iteratively improved until convergence is reached.

5.3.4. Magnitude of 2D processes

With multiple components in the 2D model capable of generating higher-order effects it is not obvious which is most important. By removing some of these forcing terms their contributions to the full solution can be quantified. In full-complexity form, MOED is initialized with u, v, F_z, F_h, $H(x)$, and sediment conductivity structure. The dominant 1D signal comes from downstream velocity (v) and the vertical magnetic field (F_z), while perturbations could arise from horizontal gradients of $\boldsymbol{u}$, horizontal gradients of σ. sloping topography, F_h, or thick and inhomogeneous sediment. Three cases with reduced forcing were solved: 1) just v and F_z with full sediment structure, 2) just F_h with u and v and full sediment structure, and 3) uniformly conductive sediment ($\sigma_s = 0.583$ S m^{-1}) with forcing from u, v, F_z and F_h.

The 2D perturbations of the depth-uniform quantity $\overline{\boldsymbol{v}}^*$ are calculated for the full-complexity and 3 reduced-complexity cases by comparison with the 1D approximation

$$\epsilon = \overline{v}^*_{2D} - \overline{v}^*_{1D} \quad , \tag{17}$$

where $\overline{\boldsymbol{v}}^*_{2D}$ is from one of the 4 model runs. Note that the 1D approximation assumes no electrical signals are generated by F_h, and so the entire electric field response is considered as the perturbation. To obtain equivalent errors in $\overline{\boldsymbol{v}}$ it would be necessary to multiply by $(1+\lambda)/(1+\gamma)$. As the appropriate values of λ and γ to use are not well-defined, errors in $\overline{\boldsymbol{v}}$ are postponed until section 5.4.3.

The quantities $\overline{v}^*_{2D}$ and ϵ for the full forcing and the 3 cases above are presented in Figure 8. Relative to the full solution the 1D approximation is accurate within 0.01 m s^{-1}, except on the upper continental shelf where the errors are roughly 0.05 m s^{-1} (20%). The negative electric field inshore of the edge of the Gulf Stream is caused by horizontal shorting of the electric potential through the thick underlying sediments. The large negative spike is located where the velocity field is set to zero (at $x = 2$ km), and the qualitative feature of negative $\overline{\boldsymbol{v}}^*$ inshore of this point will be independent of the exact velocity structure near the Gulf Stream's inshore edge.

All cases that include v and F_z recover the dominant signal and most of the 2D perturbations, implying that sloping topography and horizontal velocity gradients create most of the 2D perturbations in $\overline{\boldsymbol{v}}^*$. These two processes are hard to disentangle, given that the Gulf Stream is constrained dynamically by the continental slope. Perturbations induced by F_h are less than 0.01 m s^{-1} ($< 5\%$) everywhere, decreasing to less than 0.001 m s^{-1} seaward of the 2000-m isobath. At the 1000-m station F_h-induced perturbations are roughly half of the total perturbations.

The full-detail sediment structure is responsible for weak perturbations less than 0.02 m s^{-1}. The value of the uniform sediment conductivity (0.583 S m^{-1}) is such that the fractional deviation of $\overline{v}^*_{2D}$ for this case relative to the full-complexity solution integrates to zero over the offshore region of weak 2D perturbations ($60 < x < 120$ km). This uniform value of σ_s results in decreased sediment shorting on the upper continental slope and increased shorting on the lower continental slope. The presence of conductive coarse sand ($\sigma_s = 1.5$ S m^{-1}) on the continental shelf results in a decay length-scale inshore of $x = 2$ km that is much smaller with full sediment structure than with homogeneous sediment.

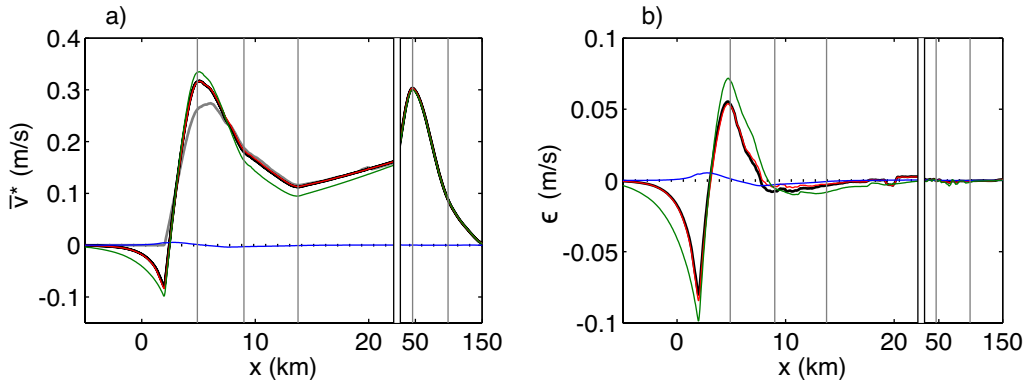

Figure 8: (a) $\bar{v}^*$ calculated for the full complexity case (thick black line), the three reduced complexity cases (u and E_z, red; u, v and F_h, blue; uniform sediment conductivity, green), and the 1D approximation $\bar{v}^*_{1D}$ (thick gray line). (b) The perturbation ϵ between the four $\bar{v}^*$ shown in (a) and $\bar{\boldsymbol{v}}^*_{1D}$. The 5 station positions are denoted by vertical gray lines, and there is a scale break at $x = 22.5$ km.

5.4. Comparison with data

The model is first evaluated by whether it accurately reproduces the AVP measurements of electric field, after which it can be used to correct the measurements for higher order perturbations.

5.4.1. Reproducing electric fields

Since the AVP only calculates $\bar{\boldsymbol{v}}^*$ over a limited depth range, namely when the Doppler system is active within 50–250 m of the seafloor, (10) needs to be applied for the model with equivalent integration ranges (namely $z_1(x) = H(x)+50$ m and $z_2(x) = H(x)+250$ m). The resulting quantity is denoted $\bar{v}^*_{2D,AVP}$. Though this choice is less general and ignores the importance of velocity above this region, such an an estimate of $\bar{\boldsymbol{v}}^*$ is directly analogous between the observations and the model. Most EM-based instruments determine or measure $\bar{v}^*$ over a limited depth range if not at a fixed depth (e.g. at the seafloor), so the results obtained for the AVP will be similar for other instruments.

Along the steep continental slope the horizontal electric field E_x (Figure 9b) is not vertically uniform because the strong field in the water doesn't penetrate to the bottom of the sediment, so this is a location where there are perturbations from the 1D approximation. The deviation from the 1D approximation is most readily seen by comparing $\bar{v}^*_{2D,AVP}$ (red) against $\bar{v}_{1D}$ (blue) in Figure 9a. It is only on the upper continental shelf that differences are larger than a few cm s^{-1}. The AVP data are within 0.02 m s^{-1} of the calculated results at all stations seaward of the 1000 m isobath. At the shallowest station, the modeled $\bar{\boldsymbol{v}}^*_{2D}$ differs by 0.05 m s^{-1} (17%) from $\bar{\boldsymbol{v}}^*_{AVP}$ and gives a result that is twice as close to the observations as the 1D approximation suggests. The 2D model is a clear improvement.

Inverting from $\bar{\boldsymbol{v}}^*$ to $\bar{\boldsymbol{v}}$ involves the factors γ and λ. Following (4), $\bar{v}(1+\gamma)$ is related to $\bar{v}^*$ in a 1D sense by a slope of $1+\lambda$ and are plotted in Figure 10 in analogy to Figure 5. The line that describes $\bar{v}^*_{2D,AVP}$ and $\bar{v}(1+\gamma)$ from the model (Figure 10a, black line) starts out at the origin at the inshore edge, $\bar{v}^*_{2D,AVP}$ becomes negative while $\bar{v} = 0$, and then both become positive and proceed through the maximum at the 500 m isobath, the local minimum at the 2000 m isobath, and finally the local maximum at the 3000 m isobath. Though the value from the model at each station is

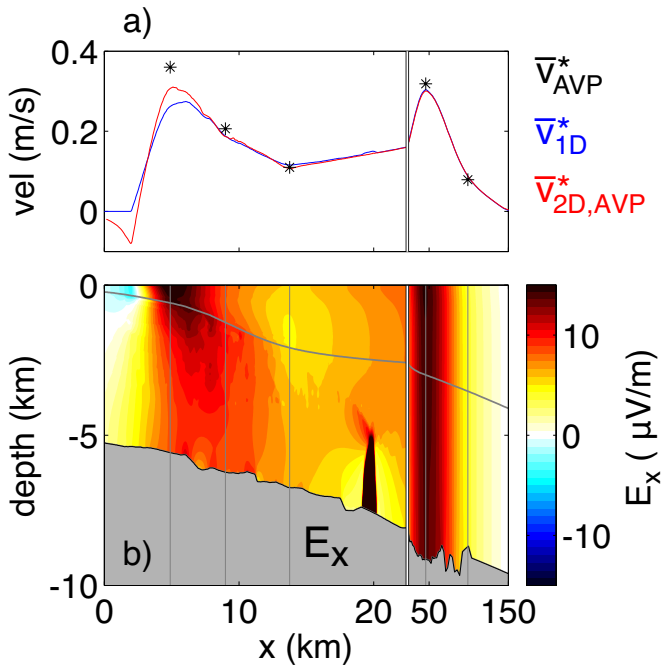

Figure 9: MOED results using AVP observations and compiled sediment conductivities. (a) Vertically-averaged quantities: $\overline{v}_{1D}$ (blue line), $\overline{\mathbf{v}}^*_{2D,AVP}$ from MOED (red line), and station-averaged AVP $\overline{v}^*$ (black *). (b) Horizontal electric field. The full sediment depth is shown, the seafloor (gray line) is in the top half and the non-conductive basement is shown by the gray shading. AVP stations are indicated by vertical lines. Note the break in horizontal scale at x = 22.5 km.

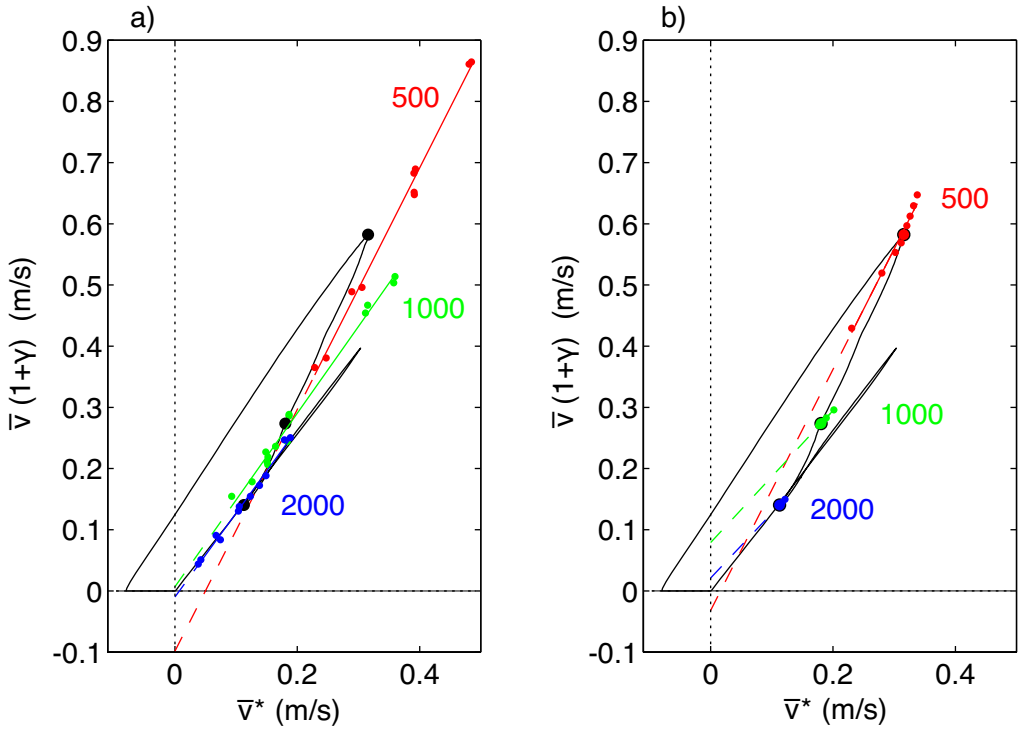

Figure 10: Graphs of $\overline{v}(1+\gamma)$ against $\overline{v}^*$. (a) The AVP data (dots for individual profiles; linear fit with a solid line with its extension to $x = 0$ as a dashed line) and the values of $\overline{v}(1+\gamma)$ and $\overline{v}_{2D,AVP}$ from MOED (black line; large black dots at the 500, 1000, and 2000 m stations from top to bottom). AVP Data at the 500 m station is shown in red, at the 1000 m station in green, and at the 2000 m station in blue. (b) Linear fits from the model results at the three stations with schematic meanders: a shift of 0 m (black line, large colored dots), shifts up to ±1000 m (small colored dots), linear fits at each station (solid line; extension to 0 as dashed line). The color coding is the same as in (a).

close to the average of the AVP data, the observations have large ranges at each station. This is reflective of Gulf Stream meanders and requires a reconsideration of the meaning of linear fits between $\overline{\boldsymbol{v}}^*$ and $\overline{\boldsymbol{v}}(1+\gamma)$.

5.4.2. Time variability of the Gulf Stream

There are two ways to recover the range of velocity $\overline{v}$ seen in the data at each station: either by inadvertently sampling the horizontal structure of the Gulf Stream, or else by the Gulf Stream meandering over topography. As there are not enough data for a fully-realistic treatment of meanders, a schematic treatment will be used instead for determining how meanders influence the interpretation of electromagnetic fields.

The first method involves sampling spatial locations of the time-invariant Gulf Stream. This describes inexact station repeats and is denoted by $()_{dx}$. The AVP stations on the continental slope have cross-stream standard deviations of 140–220 m, much smaller than the 3–5 km separation between them. Ultimately, the contribution from inexact station repeats is small: multiplying the standard deviation of cross-stream location by the horizontal gradient of $\overline{v}$ yields a range of less than 0.02 m s^{-1} for all stations. This sampling method cannot recover the strong

observed fluctuations in $\overline{\mathbf{v}}$.

The second method is by staying at a fixed location relative to topography while the velocity structure shifts horizontally to either side. This describes meandering and is denoted by $()_{dv}$. The sampling is realistically a combination of inexact repeats and meandering, but the results from combining both are very similar to those from just including the meandering.

The range of $\overline{v}$ measured by the AVP during the 5 days of measurements shows that, over the continental slope, the vertically-integrated velocity (or transport per unit width) changes direction by 35° (not shown) and magnitude by factors of 2–5 (Figure 5). While Gulf Stream meanders downstream of Cape Hatteras can be readily described by translation and rotation of the velocity structure (Watts et al., 1995), meanders at Cape Hatteras and to the south interact with the continental slope and have shorter periods and wave-lengths (Johns et al., 1995; Savidge, 2004) than to the north. Immediately south of Cape Hatteras, meanders have length scales less than 100 km and periods longer than 3 days (Savidge, 2004). Cape Hatteras separates these two eddying regimes and serves as the location where the lateral movement of the Gulf Stream's northern edge is a minimum (10 km, Olson et al., 1983; Tracey and Watts, 1986). Even so, at the 500 m isobath the Gulf Stream is 400 m deep, and thus the velocity will be modified by topography for shifts greater than 3 km inshore, the distance to the 400 m isobath.

Neither the AVP sampling nor historical observations are extensive enough to resolve how the velocity structure of the Gulf Stream evolves during meander events along the continental slope. Accordingly, meanders are treated simply as lateral shifts of the time-averaged velocity structure. This meandering mode is commonly used downstream of Cape Hatteras, and is supported at Cape Hatteras by the observations: the stations on the continental slope show a positive correlation between velocity and temperature at constant depth levels (not shown). This implies that if the center of the Gulf Stream (near $x = 45$ km) moves inshore and velocity increases that isotherms deepen and temperature rises. Since the velocity structure of large onshore meander events are not merely lateral shifts because they interact with topography in an unresolved fashion, I limit the meander amplitudes to ±1000 m. The changes that occur in $\overline{v}$ for meanders of ±1 km are shown in Figure 7a by the gray lines on either side of the unshifted value (black). A synthetic sampling from the meandering Gulf Stream model consists of data from 9 meander amplitudes: 0, ±125, ±250, ±500 and ±1000 m.

Lateral shifts of the Gulf Stream over topography have three implications for electric fields. First, the electric field depends to first order on $\overline{\mathbf{v}}(x)$, such that small horizontal meanders over steep topography result in large changes in $\overline{v}$, even if the transport per unit width $H\overline{v}$ remains constant. Second, the horizontal velocity gradients are not constant in space, and, since they are strongest over the continental slope, any meanders shift the velocity gradients relative to topography. Third, lateral meandering is distinctly different from a 'pulsing' mode in which the amplitude of the entire velocity structure changes in tandem. Though there is limited evidence that the Gulf Stream pulses, this mode is note-worthy because it corresponds exactly to that implied by (4): fluctuations in $\overline{v}(1+\gamma)$ and $\overline{v}^*$ are linearly related. In reality, fluctuations in $\overline{v}$ at Cape Hatteras arise from many concomitant changes during a meander event, so 2D perturbations at any one location will not necessarily be the same magnitude as a meander develops. The 1D contribution, however, will remain linearly related to $\overline{\mathbf{v}}$.

There are two ways of interpreting measurements of $\overline{\mathbf{v}}$ and $\overline{\mathbf{v}}^*$. In general, $\overline{\mathbf{v}}(1+\gamma)$ and $\overline{\mathbf{v}}^*$ do not maintain a constant ratio, and thus they define a line that does not go through the origin (Figure 11). The best fit line to these points is a tangent line (orange, with a slope and y-intercept), the same analysis as used to interpret the original AVP observations in section 5. Another method is a ratio fit (purple) that forces the fit to go through the origin and only has a slope (denoted as

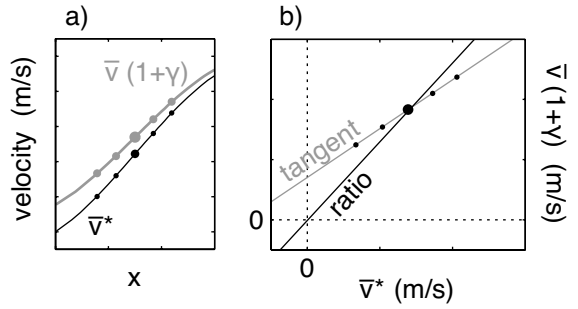

Figure 11: Schematic diagram of the fitting procedure. (a) The quantities $\bar{v}$ and $\bar{v}^*$ plotted against distance, with one central point and 2 points on either side. (b) The 5 points from panel (a) plotted for $\bar{v}(1+\gamma)$ against $\bar{v}^*$. A tangent line fit recovers a straight line that does not necessarily go through the origin, whereas a ratio fit connects the origin with the geometric mean of the data.

$(\,)_r$). This constraint causes the line to be defined by the slope to the geometric mean of the data (central large point, Figure 11b).

There are now two Gulf Stream models (time-invariant or meandering) and two interpretation methods (tangent line or ratio) to apply at Cape Hatteras. With a time-invariant Gulf Stream (denoted with a subscript dx), the tangent line fit extracts the instantaneous slope of the black line in Figure 10a: at local extrema the slope ($1 + \lambda_{\mathrm{d}x}$, red-dotted line in Figure 12) changes rapidly and goes through either 0 or ∞, while the y-intercept ($y_{0,\mathrm{d}x}$, solid red line in Figure 13) can reach large values. In contrast, the ratio fit ($\lambda_{r,\mathrm{d}x}$, red solid line in Figure 12) is smoother and less sensitive to local extrema.

With a meandering Gulf Stream (denoted with a subscript dv), the two fitting methods can not be visualized as readily from $\bar{\boldsymbol{v}}^*$ and $\bar{\boldsymbol{v}}(1+\gamma)$. The tangent line method ($1 + \lambda_{\mathrm{d}v}$, dotted blue line in Figure 12; and $y_{0,\mathrm{d}v}$, solid blue line in Figure 13) gives smoother results than with a time-invariant Gulf Stream, but it is still more variable than the ratio fit with meandering ($1 + \lambda_{\mathrm{r,d}v}$, solid blue line in Figure 12).

How well do the various models and fits agree with the AVP observations? The tangent line methods are highly variable for both λ and y_0 regardless of the Gulf Stream model. Though the tangent method with time-invariant velocity structure appears to recover the values at the 500-m and 2000-m stations, in fact both values are undefined because these locations are local extrema. Though the tangent method interpretation of a meandering Gulf Stream gives more stable results than for a time-invariant Gulf Stream, the values do not match the observations any better. There are strong reasons for desiring a smooth λ: physically, the sediment factor should be a slowly varying property because of large-scale depositional patterns and horizontal averaging of E_x on scales of 1–2 D (SzI; SzII); and methodologically, stable values of λ are needed for a robust inversion from $\bar{\boldsymbol{v}}^*$ to $\bar{\boldsymbol{v}}$. Thus, the tangent line methods are of limited use in describing the modeled EM fields at Cape Hatteras.

The ratio method, by construction, gives smoother results. Both the time-invariant and the meandering Gulf Stream models are in decent agreement with the observations and give smooth sediment ratios over the continental slope. With the additional but unresolved influence in observations of uneven sampling of meanders, the greater stability of ratio fits will give a more robust inversion for $\bar{\boldsymbol{v}}$.

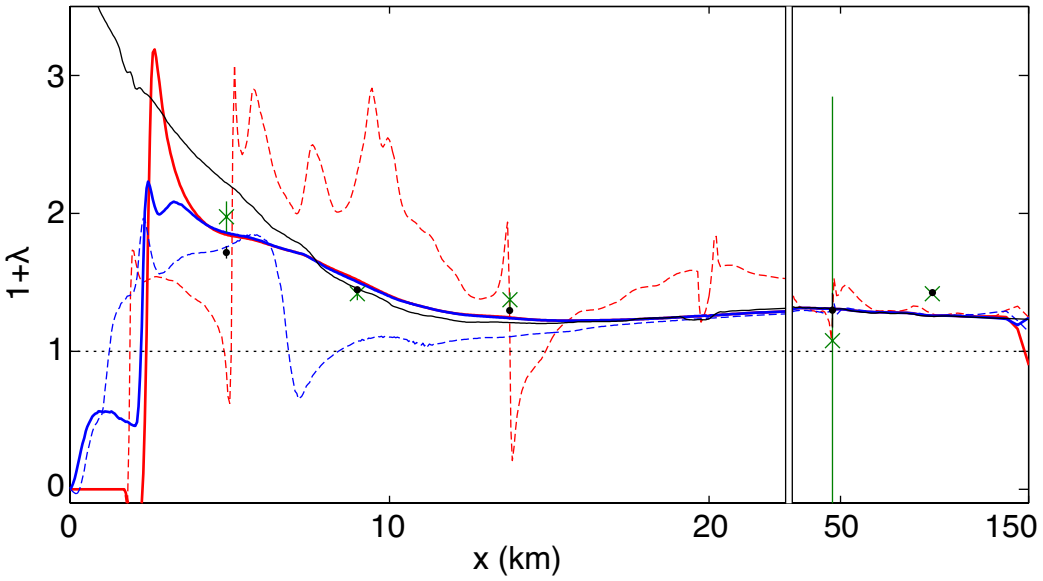

Figure 12: The quantity $1 + \lambda$: AVP data, tangent-line fit (green ×) and ratio fit (black dot) with vertical lines for 95% error bars, the 1D value $1 + \lambda_{1D}$ (black line), sampling over x with velocity fixed to topography for the ratio method $1 + \lambda_{r,dx}$ (red solid line) and the tangent line method $1 + \lambda_{dx}$ (red dotted line), sampling at one location with velocity shifting relative to topography for the ratio method $1 + \lambda_{r,dv}$ (blue solid line) and the tangent line method $1 + \lambda_{dv}$ (blue dotted line).

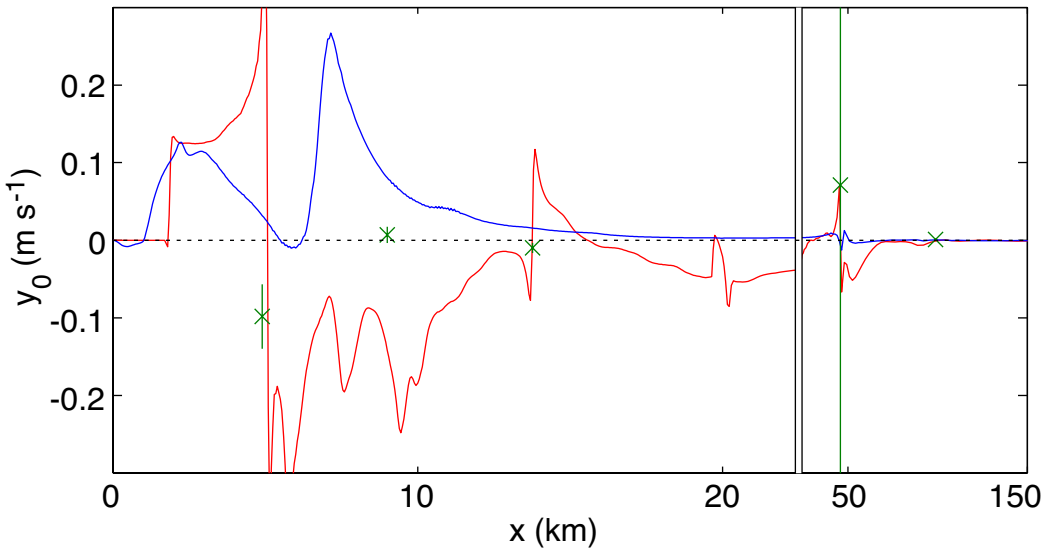

Figure 13: The y-intercept y_0: AVP data (green ×, with 95% error bars shown by green vertical lines), tangent line fit with fixed velocity $y_{0,dx}$ (red line), and tangent line fit with meandering $y_{0,dv}$ (blue line).

5.4.3. Accuracy of inverting for velocity

Now that the depth-averaged relationship between $\overline{v}$ and $\overline{v}^*$ is clearer, I consider how accurately the electric field can be inverted to velocity. A simple definition of 2D perturbations or 2D errors is used: the difference between a 1D interpretation of the 2D electric response and the true velocity. Different methods of calculating λ lead to different errors, which in turn help choose which λ is most stable and least biased for interpreting 2D electric response.

Inverting for depth-uniform velocity.

The depth-uniform error is

$$\overline{\epsilon}_i = \overline{\boldsymbol{v}}^*_{2\mathrm{D}}(1+\lambda_i)/(1+\gamma) - \overline{v} \quad , \tag{18}$$

where $\overline{v}^*_{2\mathrm{D}}$ is averaged through the entire water column. The subscript $()_i$ denotes which λ_i is used from the previous section: $i = 1\mathrm{D}$ for $\lambda_{1\mathrm{D}}$ when the sediment conductance is known exactly, $i = r, \mathrm{d}x$ for the time-invariant velocity structure analyzed with a ratio fitting approach, or $i = r, \mathrm{d}v$ for meandering velocity structure analyzed with a ratio fitting method.

The 1D theory with complete sediment knowledge ($\overline{\epsilon}_{1\mathrm{D}}$, black line, Figure 14) describes the electric field within a few cm s^{-1} over most of the Gulf Stream. The error is largest on the upper slope (maximum of 0.13 m s^{-1}, or 25% relative error) where there is a sharp inshore maximum of depth-averaged velocity. Electric fields and 2D perturbations tend to spread out relative to narrow velocity gradients, as can be seen in the positive maximum in all errors at the 500-m isobath (position indicated by the left-most green line in Figure 14) with negative extrema on either side.

Of the heuristic methods of calculating λ, the smallest depth-uniform error comes from $\lambda_{\mathrm{r,d}x}$ ($\overline{\epsilon}_{\mathrm{d}x}$, red line) based on a stationary velocity structure. Errors are less than 0.002 m s^{-1} except on the upper continental slope. These errors would apply to a near-synoptic transect, assuming that the length scales in reality are no smaller than those resolved here. For a meandering velocity structure ($\overline{\epsilon}_{\mathrm{d}v}$, blue line) the errors are larger and more variable over the entire width of the Gulf Stream. Specifically, $\overline{\epsilon}_{\mathrm{d}v}$ exhibits large depth-uniform errors near the inshore $\overline{v}$ maximum (errors less than 0.23 m s^{-1}, 50%) and moderate errors over the salt diapir at 19 km (errors of -0.05 m s^{-1}, -50%), but in other regions the error is much smaller (< 0.02 m s^{-1}, or $< 10\%$ of $\overline{v}$). Heuristic determination of sediment shorting via $\lambda_{\mathrm{r,d}v}$ leads to larger depth-averaged errors than with independent and accurate knowledge of $\lambda_{1\mathrm{D}}$. Also, $\overline{v}^*$ does not exactly follow the small-scale variations of $\overline{v}$, as can be expected from horizontal averaging arguments (SzI; SzII).

Inverting for depth-varying velocity.

Depth-varying errors in $\boldsymbol{J}_h(z)/\sigma$ have different vertical structure than the forcing velocity $\boldsymbol{v}(z)$. Because the electric current derived velocity measured by vertically-profiling instruments (the AVP in this case) is a relative velocity, the depth-varying error is defined as the difference between these two properties with the vertical mean removed

$$\begin{aligned} \epsilon'(x,z) &= v(x,z) - \frac{J_x(x,z)}{\sigma(z)F_z} - \overline{\epsilon'}(x) \\ \overline{\epsilon'} &= \frac{1}{z_2 - z_1}\int_{z_1}^{z_2}\left[v(x,z) - \frac{J_x(x,z)}{\sigma(z)F_z}\right]\mathrm{d}z \quad . \end{aligned} \tag{19}$$

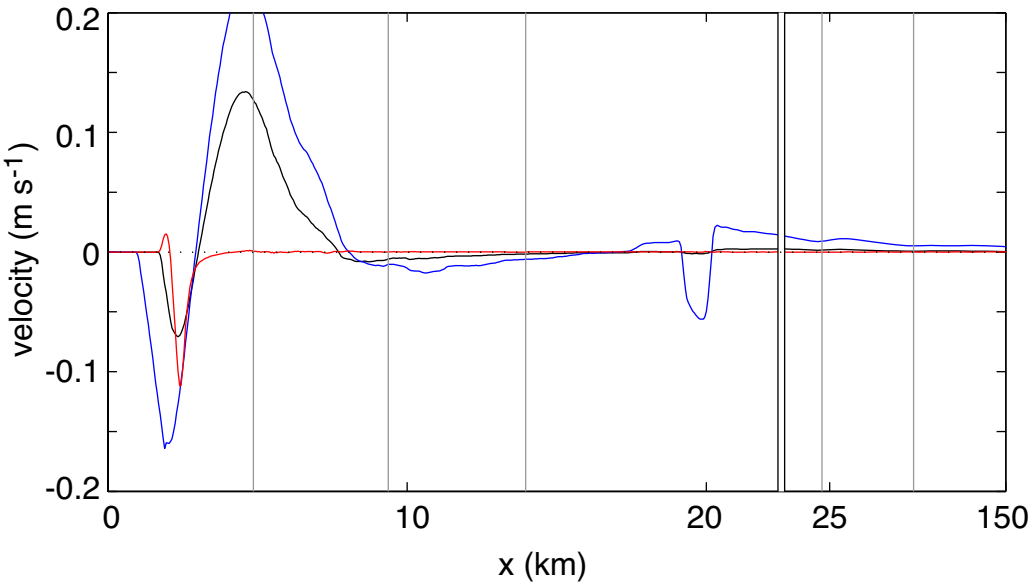

Figure 14: Depth-uniform velocity errors from (18): $\overline{\epsilon}_{1D}$ using a fully-known sediment conductance (black line), $\overline{\epsilon}_{r,dx}$ using a ratio fit for a stationary velocity structure (red line), and $\overline{\epsilon}_{r,dv}$ using a ratio fit for a meandering velocity structure (blue line). Station locations are shown by vertical gray lines. Errors from tangent line fits are highly variable and are not shown.

The removal of a vertical mean decouples the depth-uniform signal from the depth-varying error. If the integral occurs over the full water column ($z_1 = H(x)$ and $z_2 = 0$ m), then the vertical mean that is removed is equivalent to $\overline{\boldsymbol{v}}^*_{2D}$.

With $\overline{\epsilon'}$ calculated over the full water-column, the error ϵ' (Figure 15b) has maximum amplitudes but different signs at the sea surface and bottom. The vertical root mean square (rms) of ϵ' (Figure 15a) is largest on the continental slope with values of ≤ 0.02 m s^{-1} and decreases to < 0.005 m s^{-1} in deeper water.

For the AVP observations the vertical offset $\overline{\epsilon'}$ from (19), equivalent to $\overline{\boldsymbol{v}}^*_{2D,AVP}$, can only be calculated when the acoustic Doppler system is active within 50–250 m of the bottom, which adds a bias to ϵ'. At locations where the depth-varying error is significant and bottom-intensified, the AVP velocity error, denoted ϵ'_{AVP}, is increased over the entire water column by ≤ 0.01 m s^{-1} rms (purple line, Figure 15a). The depth-varying relative error is less than 10% of the depth-uniform velocity, or, given the maximum surface velocities is 1.5–2 m s^{-1}, the relative error is 1–2%.

The depth-uniform and depth-varying velocity errors tend to have maximum horizontal gradients where the velocity is constrained at the AVP stations. The griding method, despite maintaining a smooth second derivative, inherently generates smaller gradients between the stations. This implies that the model only resolves 2D perturbations defined by the 5 sampling stations, and that the true velocity structure is expected to lead to depth-varying errors of similar magnitude between the AVP stations.

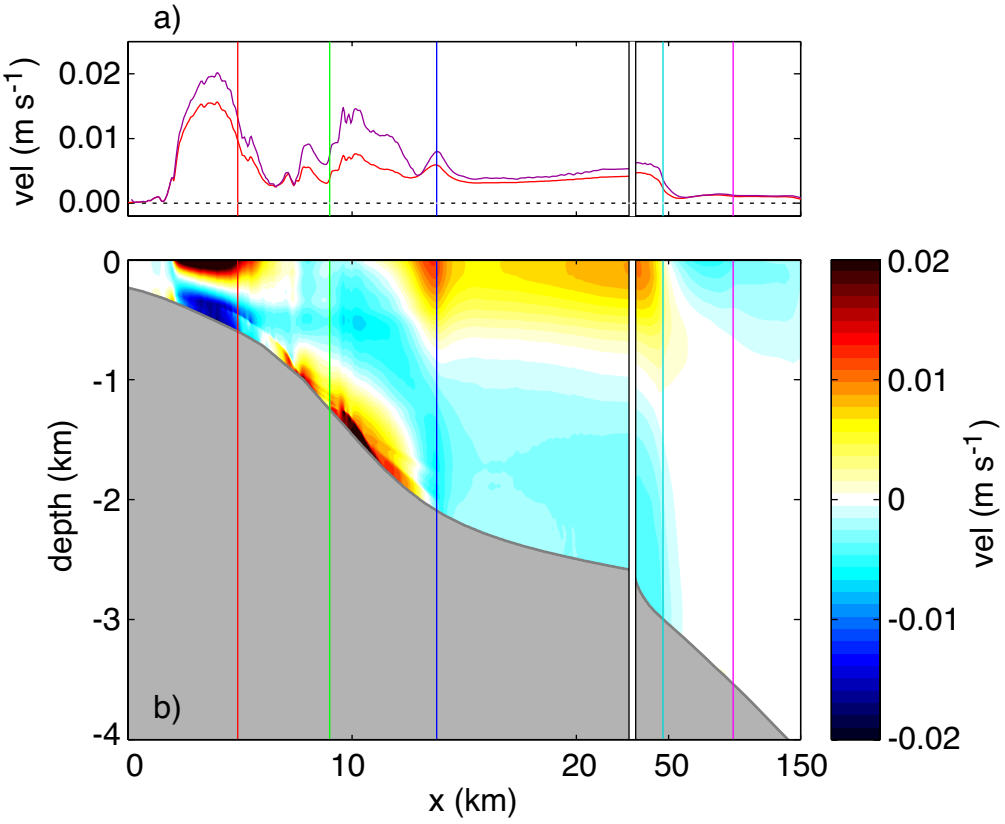

Figure 15: Depth-varying velocity errors calculated from the model output. (a) The vertical rms of $\acute{\epsilon}$ (in red) and the vertical rms of ϵ'_{AVP} (in purple). (b) Depth-varying velocity errors ϵ' (color) from (19).

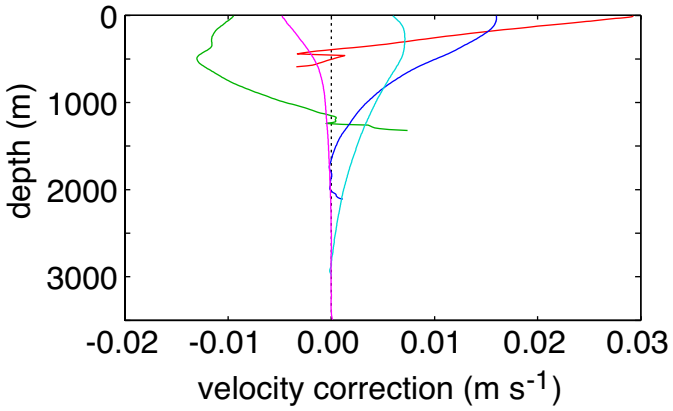

Figure 16: Correction to AVP velocities for 2D errors. Profiles of $\epsilon'_{v,\mathrm{AVP}}$ at each station. In addition to the vertical extent of the profiles, the station is indicated by the same colors as in Figure 15.

5.4.4. Iterative solution method

Having calculated the shape and magnitude of 2D perturbations for the AVP observations, I can now verify the suitability of the initial 1D interpretation of the AVP measurements used to initialize the model.

The profiles of 2D corrections needed for the time-averaged velocities ϵ'_{AVP} are shown at each station in Figure 16. The corrections are mostly less than 0.02 m s^{-1} and are correlated with the regions of strong flow. Their surface intensification, though mostly a reflection of the surface intensified Gulf Stream, is further increased by near-bottom referencing. With surface velocities of 1–1.5 m s^{-1}, these are only corrections of less than 1–2%.

Given that the velocity is accurate to first order, an iterative approach is appropriate. For the next iteration, this would entail adding ϵ'_{AVP} to the original velocity profiles and recalculating the solution. Treating the iteration as a Taylor expansion about the true 2D perturbation, the magnitude of the second iteration would be the square of 1%. As the first iteration is already equivalent to the accuracy of the instrument, no further iterations are necessary.

5.5. Discussion

The motivation for this study came from small but statistically significant inconsistencies found in a 1D interpretation of EM-derived velocity measurements at Cape Hatteras. The interpretation of a field location presented here is useful in a theoretical sense (how large are the perturbations?), as well as in a methodological sense (how can 2D perturbations be characterized and removed?)

The sampling location at Cape Hatteras was purposely chosen by Sanford et al. (1996) to invalidate the WKBJ assumptions underlying his 1D approximation (Sanford, 1971). Most of the factors that can generate 2D perturbations are found to be large here: horizontal velocity gradients, topographic slopes, total sediment thickness, inhomogeneity of sediment conductivity, and ocean flow in the direction of magnetic east-west. When this location is characterized in terms of parameter space (SzI; SzII), it occupies an extreme corner based on geophysical scaling arguments. Thus, the errors found here can be treated as an upper boundary for most parts of the ocean.

The benefit of using a numerical model to investigate 2D electromagnetic perturbations is that the strong horizontal gradients can be well resolved numerically. For comparison with reality, there are two ways in which the model results reflect the under-sampling of the AVP observations: 1) the model is initialized with higher horizontal resolution for the water depth and sediment than for velocity, and 2) the velocity observations used for initialization are time-averaged over a meander event.

The first consideration is the higher horizontal constraint of the seafloor and sediment structure compared with velocity structure. The velocity field used to initialize the model is only constrained at a few locations across the Gulf Stream. Using the exact seafloor under track lines in the model increases the noise in the results, because many of the vertically-averaged quantities (e.g. $\overline{v}$, $\overline{v}^*$, etc.) are divided by H for analysis and so will respond to the higher wavenumbers inherent in H. For this reason a highly smoothed seafloor is used in the model. By contrast, the finding that electric fields and electric currents are spatially averaged over distances of 1–2 $H(1 + \lambda)$ (Chave and Luther, 1990; SzII) suggests that this approach will recover the gross magnitude and shape of 2D perturbations. In the sense that it is difficult to fully resolve quickly varying subsurface velocity structure with any observational techniques, the inability to include such detail in motional induction theory is consistent with current observational practices.

The second consideration is that the model assumes a constant velocity structure that is undistorted by meanders. This is a necessary simplifying assumption, given the lack of studies that characterize the velocity field of Gulf Stream meanders over continental slopes. To first order, free Gulf Stream meanders involve a shift of the entire structure (Manning and Watts, 1989; Johns et al., 1995) that allow a stream-coordinate interpretation, with second-order changes related to cyclostrophic balance (Johns et al., 1989). The velocity structure for Gulf Stream meanders against topography, that is, upstream of Cape Hatteras, is less well characterized. Meanders have been observed from the surface (Miller, 1994), with expendable bathythermographs (Glenn and Ebbesmeyer, 1994), or from moored current meters (Savidge, 2004), but the velocity structure along the continental slope can only be inferred from such results.

Implementing schematic meanders by shifting the velocity structure recovers some but not all of the observed fluctuations. Schematic meanders allow a clearer analysis of the geometric relation between $\overline{\boldsymbol{v}}$ and $\overline{\boldsymbol{v}}^*$ and provide an answer for the non-zero y-intercept found at the 500-m station. On the continental slope, such crude meanders give weaker fluctuations of $\overline{\boldsymbol{v}}$ than seen in the observations, and so the 2D perturbations there may be underestimated by this approach. With the limitations already imposed by the sparse station spacing, however, the general shape of the 2D perturbations is expected to be representative of reality, if not also its magnitude at most locations aside from the upper continental slope.

Another way to regard the temporal averaging is that velocity extrema and horizontal velocity gradients are not fixed in stream coordinates or relative to topography, but rather, any one location in stream coordinates can have a range of velocities, velocity gradients, or bottom slopes over the course of a meander event. Thus, 2D perturbations may vary as much as the velocity field, and it is expected that observational errors and noise are reduced by time-averaging as much as by explicit horizontal smoothing used for initializing the model.

The large values in the depth-uniform velocity error found at the 500-m isobath are unexpectedly large. Although the true error is unknown for lack of knowledge of the inshore velocity field, the sensitivity to Gulf Stream meanders and to the width and location of the inshore velocity front is large. Depth-uniform errors are 0.05–0.25 m s $^{-1}$ for a range of meander amplitudes and for a range of widths (1–5 km) over which the velocity decreases to zero inshore from the 500-m isobath (results not shown). Errors are minimal when the sediment electrical properties

are fully known. More practically, heuristically recovering the effect of sediment via λ is shown to be more stable using a ratio fit than a tangent line fit. Not surprisingly, meanders increase the depth-uniform errors.

The magnitude of errors found at Cape Hatteras with a full-complexity EM model can be compared to idealized studies of higher order EM perturbations. The geometry at 500-m can be roughly described by the non-dimensional parameters investigated in SzI and SzII. These two studies investigate three specific causes for 2D perturbations: horizontal velocity gradients and induction by F_z, horizontal velocity gradients and induction by F_x, and topographic gradients and induction by F_z. These studies investigate perturbations caused by horizontal velocity gradients and sloping topography in isolation, and so they do not consider whether interactions between velocity and topography may increase 2D electromagnetic perturbations.

Based on geometric scales appropriate for the 500-m station (specifically $L = 5$ km), the 2D perturbations are predominantly explained by velocity gradients and F_z for the depth-uniform error (0.20 m s^{-1} calculated in this study, 0.17 m s^{-1} estimated in SzI) and from velocity gradients and F_x for the depth-varying error (0.03 m s^{-1} calculated in this study, 0.04 m s^{-1} estimated in SzII). Although the influence of topographic slope is estimated as being an order of magnitude smaller than the effects of horizontal velocity gradients (SzII), the separation of the role of topography and velocity is not possible from the results presented here.

In the case study presented here, the contribution to the depth-uniform error from F_H is 10% that from F_z, while the impact of inhomogeneous sediment over the continental slope is 25% that from F_z, or a few cm s^{-1}. The perturbations at the 1000-m isobath and deeper are less than 0.01–0.02 m s^{-1} for all forcings.

Other profiling or Lagrangian instruments will have similar errors to those found for the AVP. Instruments on the seafloor will have larger quantitative differences because 2D perturbations are largest at the surface and bottom of the water column. Despite finding large but instantaneous depth-uniform errors from the model results, seafloor instruments measure time-series from which tides and magnetotelluric signals need to be removed prior to analysis. These frequency bands overlap with time-scales of ocean motion, for instance the time-scales on which meanders develop. Taken together, the impact of data-processing on 2D perturbations from seafloor time-series would require a more detailed analysis than undertaken here.

5.6. Conclusion

After decades of development and field experience with electromagnetic sensors designed to calculate water motion, the electromagnetic signals are well understood and the measurement capabilities have been proven. The detailed study presented here is reassuring, in that subtidal flows generate EM signals that are within a few centimeters per second of the 1D approximation in all but the most extreme situations.

The 1D approximation is used to interpret EM observations and describes a local relationship in the vertical between velocity and EM fields. There are two types of signals, vertically-averaged and vertically-varying, both of which can be exploited for indirectly measuring ocean velocity. When present, seafloor sediment affects the depth-uniform response and can be characterized from geophysical observations or by heuristic analysis of the depth-averaged velocity and electric fields.

A detailed case study at Cape Hatteras found that the 1D approximation describes the sampled electric fields to within a few percent (a few cm s^{-1}) at almost all locations. The only significant 2D perturbations occurred in the depth-uniform signal when barotropic flow meandered over topography at the inshore edge of the Gulf Stream. These perturbations are calculated

from an EM model, however, and so need to be confirmed by direct measurements. At other locations along the transect, and in all of the depth-varying fields sampled by profiling floats, the 1D approximation resulted in errors less than 1–2 cm s^{-1}. These interpretational errors are the same order of magnitude as instrumental accuracy. The joint effect of steep bathymetry and horizontal velocity gradients yields the same magnitude of errors as found by a linear and separate analysis of the two effects (SzI; SzII)

Given the extreme nature of the sampling location in terms of invalidating the assumptions behind the 1D approximation, 2D perturbations in most parts of the ocean will be significantly smaller than found here. Accordingly, the 1D approximation is sufficient for interpreting subtidal motionally induced signals at almost all locations.

Acknowledgments. This research benefited greatly from the guidance of Tom Sanford at all stages of the project. Discussions with him, Eric D'Asaro, and James Girton brought much clarity to the final results. Rob Tyler graciously allowed use of his numerical model MOED, which enabled the detailed analysis herein. This work was supported by NSF grant 0552139.

References

Althaus, A.M., Kunze, E., Sanford, T.B., 2003. Internal tide radiation from Mendocino Escarpment. J. Phys. Oceanogr. 33, 1510–1527.

Aprea, C., Unsworth, M.J., Booker, J., 1998. Resistivity structure of the Olympic Mountains and Puget Sound Lowlands. Geophys. Res. Lett. 25, 109–112.

von Arx, W.S., 1950. An electromagnetic method for measuring the velocities of ocean currents from a ship under way. Papers in Physical Oceanography and Meteorology, MIT/WHOI 11, 1–62.

Baringer, M.O., Larsen, J.C., 2001. Sixteen years of Florida Current transport at 27°N. Geophys. Res. Lett. 28, 3179–3182.

Bowden, K.F., 1956. The flow of water through the Straits of Dover related to wind and differences in sea level. Philos. T. Roy. Soc. A 248, 517–551.

Bretherton, C.S., Widmann, M., Dymnikov, V.P., Wallace, J.M., Bladé, I., 1999. The effective number of spatial degrees of freedom of a time-varying field. J. Climate 12, 1990–2009.

Chave, A.D., Filloux, J.H., Luther, D.S., Law, L.K., White, A., 1989. Observations of motional electromagnetic fields during EMSLAB. J. Geophys. Res. 94, 14153–14166.

Chave, A.D., Luther, D.S., 1990. Low-frequency, motionally induced electromagnetic fields in the ocean: 1. Theory. J. Geophys. Res. 95, 7185–7200.

Chave, A.D., Luther, D.S., Filloux, J.H., 1992. The Barotropic Electromagnetic and Pressure Experiment 1. barotropic current response to atmospheric forcing. J. Geophys. Res. 97, 9565–9593.

Chave, A.D., Luther, D.S., Filloux, J.H., 1997. Observations of the boundary current system at 26.5°N in the Subtropical North Atlantic Ocean. J. Phys. Oceanogr. 27, 1827–1848.

Chave, A.D., Luther, D.S., Meinen, C.S., 2004. Correction of motional electric fields measurements for galvanic distortion. J. Atmos. Oceanic Technol. 21, 317–330.

Climode Group, 2009. The Climode field campaign: Observing the cycle of convection and restratification over the Gulf Stream. B. Am. Meteorol. Soc. 90, 1337–1350.

Constable, S., Srnka, L.J., 2007. An introduction to marine controlled-source electromagnetic methods for hydrocarbon exploration. Geophysics 72, WA3–WA12.

Crona, L., Fristedt, T., Lundberg, P., Sigray, P., 2001. Field tests of a new type of graphite-fiber electrode for measuring motionally induced voltages. J. Atmos. Oceanic Technol. 18, 92–99.

Cunningham, S.A., Kanzow, T., Rayner, D., Baringer, M.O., Johns, W.E., Marotzke, J., Longworth, H.R., Grant, E.M., Hirschi, J.J.M., Beal, L.M., Meinen, C.S., Bryden, H.L., 2007. Temporal variability of the Atlantic meridional overturning circulation at 26.5 degrees N. Science 317, 935–938.

D'Asaro, E.A., Sanford, T.B., Niiler, P.P., Terrill, E.J., 2007. Cold wake of Hurricane Frances. Geophys. Res. Lett. 34, L15609.

Dillon, W.P., Lee, M.W., Coleman, D.F., 1994. Identification of marine hydrates *in situ* and their distribution off the Atlantic coast of the United States, in: Sloan, Jr, E.D., Happel, J., Hnatow, M.A. (Eds.), International Conference on Natural Gas Hydrates. New York Academy of Sciences, New York, NY. volume 715 of *Annals of the New York Academy of Sciences*, pp. 364–380.

Edwards, R.N., 2005. Marine controlled source electromagnetics: Principles, methodologies, future commercial applications. Surv. Geophys. 26, 675–700.
Egbert, G.D., Bennet, A.F., Foreman, M.G.G., 1994. TOPEX/POSEIDON tides estimated using a global inverse model. J. Geophys. Res. 99, 24821–24852.
Ellis, M., Evans, R.L., Hutchinson, D.R., Hart, P., Gardner, J., Hagen, R., 2008. Electromagnetic surveying of seafloor mounds in the Gulf of Mexico. Mar. Petrol. Geol. 25, 960–968.
Evans, R.L., 2007. Using controlled source electromagnetic techniques to map the shallow section of seafloor: From the coastline to the edges of the continental slope. Geophysics 72, 105–116.
Faraday, M., 1832. The Bakerian lecture: Experimental researches in electricity. second series. Philos. T. Roy. Soc. 122, 163–194.
Filloux, J.H., 1967. Oceanic electric currents, geomagnetic variations, and the deep electrical conductivity structure of the ocean-continent transition of central California. Ph.D. thesis. University of California, San Diego.
Filloux, J.H., Law, L.K., Yukutake, T., Segawa, J., Hamano, Y., Utada, H., White, A., Chave, A.D., Tarits, P., Green, A.W., 1989. OFFSHORE EMSLAB: objectives, experimental phase and early results. Phys. Earth Planet. In. 53, 422–431.
Filloux, J.H., Luther, D.S., Chave, A.D., 1991. Update on seafloor pressure and electric field observations from the North-Central and Northeastern Pacific: Tides, infratidal fluctuations, and barotropic flow, in: Parker, B.B. (Ed.), Tidal Hydrodynamics. John Wiley & Sons, Inc., New York, NY. chapter 31, pp. 617–640.
Flosadóttir, Á.H., Larsen, J.C., Smith, J.T., 1997. Motional induction in North Atlantic circulation models. J. Geophys. Res. 102, 10353–10372.
Gille, S.T., Speer, K., Ledwell, J.R., Garabato, A.N.G., 2007. Mixing and stirring in the Southern Ocean. EOS T. Am. Geophy. Un. 88, 382.
Girton, J.B., Sanford, T.B., Käse, R.H., 2001. Synoptic sections of the Denmark Strait Overflow. Geophys. Res. Lett. 28, 1619–1622.
Glenn, S.M., Ebbesmeyer, C.C., 1994. The structure and propagation of a Gulf Stream frontal eddy along the North Carolina shelf break. J. Geophys. Res. 99, 5029–5046.
Halliday, D., Resnick, R., Walker, J., 1997. Fundamentals of Physics extended. John Wiley & Sons, Inc., New York, NY. 5th edition edition.
Hughes, P., 1969. Submarine cable measurements of tidal currents in the Irish sea. Limnol. Oceanogr. 14, 269–278.
Hutchinson, D.R., Poag, C.W., Popenoe, P., 1995. Geophysical Database of the East Coast of the United States: Southern Atlantic Margin — Stratigraphy and Velocity from Multichannel Seismic Profiles. Technical Report 95–27. U.S. Geological Survey. Woods Hole, MA.
Johns, E., Watts, D.R., Rossby, T.H., 1989. A test of geostrophy in the Gulf Stream. J. Geophys. Res. 94, 3211–3222.
Johns, W.E., Shay, T.J., Bane, J.M., Watts, D.R., 1995. Gulf Stream structure, transport, and recirculation near 68°W. J. Geophys. Res. 100, 817–838.
Johnson, G.C., Sanford, T.B., Baringer, M.O., 1994. Stress on the Mediterranean outflow plum: 1. velocity and water property measurements. J. Phys. Oceanogr. 24, 2072–2083.
Kim, K., Lyu, S.J., Kim, Y.G., Choi, B.H., Taira, K., 2004. Monitoring volume transport through measurements of cable voltage across the Korea Strait. J. Atmos. Oceanic Technol. 21, 671–682.
Korhonen, J.V., Fairhead, J.D., Hamoudi, M., Hemant, K., Lesur, V., Mandea, M., Maus, S., Purucker, M.E., Ravat, D., Sazonova, T., Thébault, E., 2007. Magnetic Anomaly Map of the World. Commission for Geological Map of the World, GTK, Helsinki. first edition.
Kuvshinov, A., Olsen, N., 2006. A global model of mantle conductivity derived from 5 years of CHAMP, ørsted, and SAC-C magnetic data. Geophys. Res. Lett. 33, L18301.
Kuvshinov, A.V., Olsen, N., Avdeev, D.B., Pankratov, O.V., 2002. Electromagnetic induction in the oceans and the anomalous behavior of coastal C-responses for periods up to 20 days. Geophys. Res. Lett. 29.
Larsen, J.C., 1968. Electric and magnetic fields induced by deep sea tides. Geophys. J. Int. 16, 40–70.
Larsen, J.C., 1971. The electromagnetic field of long and intermediate water waves. J. Mar. Res. 29, 28–45.
Larsen, J.C., 1992. Transport and heat flux of the Florida Current at 27°N derived from cross-stream voltages and profiling data: theory and observations. Philos. T. Roy. Soc. A 338, 169–236.
Larsen, J.C., Sanford, T.B., 1985. Florida Current volume transport from voltage measurements. Science 227, 302–304.
Laske, G., Masters, G., 1997. A global digital map of sediment thickness. EOS T. Am. Geophy. Un. 78, F483.
Lee, C.M., Kunze, E., Sanford, T.B., Nash, J.D., Merrifield, M.A., Holloway, P.E., 2006. Internal tides and turbulence along the 3000-m isobath of the Hawaiian Ridge. J. Phys. Oceanogr. 36, 1148–1164.
Longuet-Higgins, M.S., Stern, M.E., Stommel, H., 1954. The Electrical Fields Induces by Ocean Currents and Waves, with Applications to the Method of Towed Electrodes. *Papers in Physical Oceanography and Meteorology* **13**(1). Woods Hole Oceanographic Institution/Massachusetts Institute of Technology. 37 pp.
Luther, D.S., Chave, A.D., 1993. Observing integrating variables in the ocean, in: Proceedings of the 7th Annual 'Aha Huliko'a Hawai'ian Winter Workshop on Statistical Methods in Physical Oceanography, University of Hawai'i. pp.

103–129.
Luther, D.S., Filloux, J.H., Chave, A.D., 1991. Low-frequency, motionally induced electromagnetic fields in the ocean: 2. Electric field and Eulerian current comparison. J. Geophys. Res. 96, 12797–12814.
Manning, J.P., Watts, D.R., 1989. Temperature and velocity structure of the Gulf Stream northeast of Cape Hatteras: Modes of variability. J. Geophys. Res. 94, 4879–4890.
Manoj, C., Kuvshinov, A., Maus, S., Lühr, H., 2006. Ocean circulation generated magnetic signals. Earth Planets Space 58, 429–437.
Markson, R., 2007. The global circuit intensity: Its measurement and variation over the last 50 years. B. Am. Meteorol. Soc. 88, 223–241.
Maus, S., Lühr, H., Rother, M., Hemant, K., Balasis, G., Ritter, P., Stolle, C., 2007. Fifth-generation lithospheric magnetic field model from CHAMP satellite measurements. Geochem. Geophy. Geosy. 8, Q05013.
Maus, S., Macmillan, S., Chernova, T., Choi, S., Dater, D., Golovkov, V., Lesur, V., Lowes, F., Lühr, H., Mai, W., McLean, S., Olsen, N., Rother, M., Sabaka, T.J., Thomson, A., Zvereva, T., 2005. The 10th-generation International Geomagnetic Reference Field. Geophys. J. Int. 161, 561–565.
Maus, S., Rother, M., Hemant, K., Stolle, C., Lühr, Hermannr, H., Kuvshinov, A., Olsen, N., 2006. Earth's lithospheric magnetic field determined to spherical harmonic degree 90 from CHAMP satellite measurements. Geophys. J. Int. 164, 319–330.
Meinen, C.S., Baringer, M.O., Garcia, R.F., 2010. Florida Current transport variability: an analysis of annual and longer-period signals. Deep-Sea Res. Pt. I 57, 835–846.
Meinen, C.S., Luther, D.S., Watts, D.R., Chave, A.D., Tracey, K.L., 2003. Mean stream coordinates structure of the Sub-antarctic Front: Temperature, salinity and absolute velocity. J. Geophys. Res. 108. 3263, doi:10.1029/2002JC001545.
Meinen, C.S., Luther, D.S., Watts, D.R., Tracey, K.L., Chave, A.D., Richman, J., 2002. Combining inverted echo sounder and horizontal electric field recorder measurements to obtain absolute velocity profiles. J. Atmos. Oceanic Technol. 19, 1653–1664.
Miller, J.L., 1994. Fluctuations of Gulf Stream frontal position between Cape Hatteras and the Straits of Florida. J. Geophys. Res. 99, 5057–5064.
Nilsson, J.A.U., Sigray, P., Tyler, R.H., 2007. Geoelectric monitoring of wind-driven barotropic transports in the Baltic Sea. J. Atmos. Oceanic Technol. 24, 1655–1664.
Olson, D.B., Brown, O.B., Emmerson, S.R., 1983. Gulf Stream frontal statistics from Florida Straits to Cape Hatteras derived from satellite and historical data. J. Geophys. Res. 88, 4569–4577.
Polzin, K.L., Kunze, E., Hummon, J., Eric, F., 2002. The finescale response of lowered ADCP velocity profiles. J. Atmos. Oceanic Technol. 19, 205–224.
Popenoe, P., 1985. Cenozoic depositional and structural history of the North Carolina margin from seismic-stratigraphic analyses, in: Poag, C.W. (Ed.), Geologic Evolution of the United States Atlantic Margin. Van Nostrand Reinhold, New York, NY. chapter 4, pp. 125–188.
Prandle, D., 1979. Anomalous results for tidal flow through the Pentland Firth. Nature 278, 541–542.
Preisendorfer, R.W., Larsen, J.C., Sklarz, M.A., 1974. Electromagnetic fields induced by plane-parallel internal and surface ocean waves. Technical Report HIG-74-7. Hawaii Institute of Geophysics, University of Hawaii.
Robinson, I.S., 1976. A theoretical analysis of the use of submarine cables as electromagnetic oceanographic flowmeters. Philos. T. Roy. Soc. A 280, 355–396.
Ross, C.K., 1984. Temperature-salinity characteristics of the "overflow" water in Denmark Strait during "OVERFLOW '73". Rap. Proces 185, 111–119.
Sanford, T.B., 1971. Motionally induced electric and magnetic fields in the sea. J. Geophys. Res. 76, 3476–3492.
Sanford, T.B., Allison, M.D., Dunlap, J.H., Stahr, F.R., Verrall, J.A., 1996. R/V *Endeavor* 239: Cruise Report and Preliminary Results. Tech. Rep. 9603. Applied Physics Lab, University of Washington. Seattle, WA.
Sanford, T.B., Drever, R.G., Dunlap, J.H., 1978. A velocity profiler based on the principles of geomagnetic induction. Deep-Sea Res. 25, 183–210.
Sanford, T.B., Drever, R.G., Dunlap, J.H., 1985. An acoustic Doppler and electromagnetic velocity profiler. J. Atmos. Oceanic Technol. 2, 110–124.
Sanford, T.B., Drever, R.G., Dunlap, J.H., D'Asaro, E.A., 1982. Design, operation, and performance of an expendable temperature and velocity profiler (XTVP). Tech. Rep. 8110. Applied Physics Lab, University of Washington. Seattle, WA.
Sanford, T.B., Price, J.F., Girton, J.B., 2011. Upper ocean response to Hurricane Frances (2004) observed by profiling EM-APEX floats. J. Phys. Oceanogr. 41, 1041–1056.
Sanford, T.B., Price, J.F., Girton, J.B., Webb, D.C., 2007. Highly resolved observations and simulations of the ocean response to a hurricane. Geophys. Res. Lett. 34, L13604.
Savidge, D.K., 2004. Gulf Stream meander propagation past Cape Hatteras. J. Phys. Oceanogr. 34, 2073–2085.
Schwiderski, E.W., 1979. Global Ocean Tides. Technical Report 79-414. U.S. Naval Surface Weapons Center. Dahlgren, VA.

Simpson, F., Bahr, K., 2005. Practical Magnetotellurics. Cambridge University Press, Cambridge, United Kingdom.
Smith, W.H.F., Sandwell, D.T., 1997. Global seafloor topography from satellite altimetry and ship depth soundings. Science 277, 1957–1962.
Spain, P., Sanford, T.B., 1987. Accurately monitoring the Florida Current with motionally induced voltages. J. Mar. Res. 15, 599–608.
Stahr, F.R., Sanford, T.B., 1999. Transport and bottom boundary later observations of the North Atlantic Deep Western Boundary Current at the Blake Outer Ridge. Deep-Sea Res. Pt. II 46, 205–243.
Stommel, H., 1948. The theory of the electric field in deep ocean currents. J. Mar. Res. 7, 386–392.
Szuts, Z.B., 2004. Electric Field Floats in the North Atlantic Current: Validation and Observations. Technical Report APL-UW 0405. Applied Physics Lab, University of Washington.
Szuts, Z.B., 2008. The Interpretation of Motionally Induced Electric Fields in Oceans of Complex Geometry. Ph.D. thesis. School of Oceanography, University of Washington. Seattle, WA.
Szuts, Z.B., 2010a. The relationship between ocean velocity and motionally-induced electrical signals, part 1: in the presence of horizontal velocity gradients. J. Geophys. Res. 115.
Szuts, Z.B., 2010b. The relationship between ocean velocity and motionally-induced electrical signals, part 2: in the presence of topographic slopes. J. Geophys. Res. 115.
Szuts, Z.B., Sanford, T.B., in review, 2011. Vertically-averaged velocity in the North Atlantic Current from field trials of electromagnetic instruments. Deep-Sea Res. Pt. II .
Tinsely, B.A., Burns, G.B., Zhou, L., 2007. The role of the global electric circuit in solar and internal forcing of clouds and climate. Adv. Space Res. 40, 1126–1139.
Tracey, K.L., Watts, D.R., 1986. On Gulf Stream meander characteristics near Cape Hatteras. J. Geophys. Res. 91, 7587–7602.
Tucholke, B.E., 1986. Structure of basement and distribution of sediments in the western North Atlantic Ocean, in: Vogt, P.R., Tucholke, B.E. (Eds.), The Western North Atlantic Region. Geological Society of America, Inc., Boulder, CO, pp. 331–340.
Tyler, R.H., 2005. A simple formula for estimating the magnetic fields generated by tsunami flow. Geophys. Res. Lett. 32. L09608, doi:10.1029/2005GL022429.
Tyler, R.H., Maus, S., Lühr, H., 2003. Satellite observations of magnetic fields due to ocean tidal flow. Science 299, 239–241.
Tyler, R.H., Mysak, L.A., 1995a. Electrodynamics in a rotating frame of reference with application to global ocean circulation. Can. J. Phys. 73, 393–402.
Tyler, R.H., Mysak, L.A., 1995b. Motionally-induced electromagnetic fields generated by idealized ocean currents. Geophys. Astro. Fluid 80, 167–204.
Tyler, R.H., Mysak, L.A., Oberhuber, J.M., 1997. Electromagnetic fields generated by a 3-D global ocean circulation. J. Geophys. Res. 102, 5531–5551.
Tyler, R.H., Vivier, F., Li, S., 2004. Three-dimensional modelling of ocean electrodynamics using gauged potentials. Geophys. J. Int. 158, 874–887.
Vivier, F., Maier-Reimer, E., Tyler, R.H., 2004. Simulations of magnetic fields generated by the Antarctic Circumpolar Current at satellite altitude: Can geomagnetic measurements be used to monitor the flow? Geophys. Res. Lett. 31. L10306, doi:10.1029/2004GL019804.
Watts, D.R., Tracey, K.L., Bane, J.M., Shay, T.J., 1995. Gulf Stream path and thermocline structure near 74°W and 68°W. J. Geophys. Res. 100, 18291–18312.
Wertheim, G.K., 1954. Studies of the electric potential between Key West, Florida and Havana, Cuba. EOS T. Am. Geophy. Un. 35, 872–882.
Winkel, D.P., Gregg, M.C., Sanford, T.B., 1996. Resolving oceanic shear and velocity with the Multi-Scale Profiler. J. Atmos. Oceanic Technol. 13, 1046–1072.
Winkel, D.P., Gregg, M.C., Sanford, T.B., 2002. Patterns of shear and turbulence across the Florida Current. J. Phys. Oceanogr. 32, 3269–3285.
You, Y., 2010. Opinion: Harnessing telecoms cables for science. Nature 466, 690–691.
Zedler, S.E., Niiler, P.P., Stammer, D., Terrill, E., Morzel, J., 2009. Ocean's response to Hurricane Frances and its implications for drag coefficient parameterization at high wind speeds. J. Geophys. Res. 114, C04016.